

RESPONSE TO REFEREE #1:

We thank Referee #1 for taking the time to review the manuscript and provide valuable and constructive feedback. The referee's comments are reproduced in bold; excerpts from the revised manuscript are in red type.

P2, line 41: "Lidar can detect wind velocity in clear air, but cannot work during precipitation." In fact, it has been well demonstrated that horizontal wind speed can be correctly measured in rain.

We have modified the manuscript as follows:

Emitted laser light is scattered by fine aerosol particles in the atmosphere; the back-scattered light is condensed by telescopes and received by an optical transceiver. Since the wavelength of the received light varies according to the velocity of the aerosol particles due to the Doppler effect, wind speed can be calculated by comparing this wavelength with that of the received light (Inokuchi and Akiyama, 2019). However, when rain is too heavy, the backscattering signal is weakened due to strong attenuation by raindrops and a decrease in aerosols (Wei et. al 2019), making it difficult to measure the wind velocity at a distance.

P7, line 193: the authors should list the possible physical origins of the random noise sources in their proposed lidar observation method.

We have modified the manuscript as follows:

The random noise is caused by the reduced intensity of the received light due to the thin aerosol concentration in the sky. A general Lidar signal consists of random noise superimposed on the spectral signal. If the signal intensity is low, random noise may be detected by peak search. (Additional randomness caused by environmental factors and data processing in Lidar is considered here as randomness of the wind-speed values.)

P21, line 428: "Flight demonstrations are to be performed in 2021. The results of this research will be applied to this flight demonstration." If possible, it would be useful and interesting if the authors can provide some more detail of their proposed experimental campaign.

We have modified the manuscript as follows:

Currently, the Lidar system is being modified to be smaller and lighter in order to suit small experimental aircraft. The onboard Lidar system and real-time airflow-vector estimation will be validated by flight experiments in 2021; the whole gust-alleviation system, including preview control, will be demonstrated in 2022. The results of this research will be applied to this flight demonstration.

P3, line 95: "Lidars are assumed to be compliant..."

We have modified the manuscript as follows:

The Lidars are assumed to be compliant with the specifications for preview control currently under development by the JAXA.

P4, line 121: "the estimation accuracy of the vertical wind velocity is required to be lower than 2.6 ms⁻¹ in the LOS distance of 500 m" – I suggest use of the word "better" rather than "lower".

We have modified the manuscript as follows:

... the estimation accuracy of the vertical wind velocity must be better than 2.6 m s⁻¹ ...

P11, line 258: “opening size of optical antenna” – specify radius or diameter?

We have modified the manuscript as follows:

The Lidar sensor is shown in Fig. 2; its specifications are given in Table 1 (Inokuchi and Akiyama 2019). Laser pulses generated by an optical transceiver are amplified by optical amplifiers (Sakimura et. al. 2013) incorporated into an optical antenna and radiated into the atmosphere from optical telescopes. The heat generated by the optical amplifiers is dissipated by a chiller unit using water as a coolant. The optical antenna is equipped with a 150 mm large-aperture telescope for long range observations and a 50 mm small-aperture telescope for vector conversion of short-range observations.

The approach of combining lidar returns from different times does have some similarities with a method previously demonstrated by the ZHAW group and it is worth citing the following presentation, slide 51:

https://presentations.copernicus.org/EMS2017/EMS2017-322_presentation.pdf

We have modified the manuscript as follows:

Neininger, B.: Trends in airborne atmospheric observations, European Meteorological Society Annual Meeting 2017, 14, EMS2017-322, 2017

RESPONSE TO REFEREE #2:

We thank Referee #2 for taking the time to review the manuscript and provide valuable and constructive feedback. The referee's comments are reproduced in bold; **excerpts from the revised manuscript are in red type.**

Specific Comments

a) Line 27: Add a reference to this 2014 FAA study or report.

We have modified the manuscript as follows:

For both fatal and non-fatal aircraft accidents, the impact of atmospheric turbulence can be significant. The Japan Transport Safety Board has stated that accidents caused by turbulence accounted for 48% of non-fatal aircraft accidents in Japan involving commercial airplanes from 2003-2012. An increase in the rate of accidents related to turbulence was reported by the Federal Aviation Administration in 2006, Kim and Chun in 2011, and Williams in 2017.

b) Line 28: How many fatal accidents were observed in this time frame?

We have modified the manuscript as follows:

Statistics reported by Boeing (2018) show that 322 non-fatal and 51 fatal accidents occurred worldwide in commercial jet flights from 2009 through 2018.

c) Line 34: Are these turbulence-related accidents results in LOC-I? I don't exactly follow the logic presented here, and if LOC-I accidents are related to CAT (which is the main topic of the paper). Please clarify how statistics in this whole paragraph are related to each other and relevant.

Aircraft accidents are often caused by a combination of factors that are difficult to completely identify. LOC-I can be caused by human factors, environmental factors, system factors, or a combination of these. First, the statistics show that wind phenomena (wind shear and atmospheric turbulence) are significant factors in LOC-I. Second, the statistics of aircraft accidents in Japan show the atmospheric turbulence is the largest factor in non-fatal accidents in Japan. Although non-fatal accidents (mentioned in the Japanese statistics) and fatal ones (mentioned in the LOC-I statistics) are quite different in their impact, turbulence affects both. Non-fatal accidents include events such as broken bones in passengers not wearing their seat belts and burns from spilling hot coffee while serving a cabin attendant.

We have modified the manuscript as follows:

Atmospheric turbulence poses a potential risk to aircraft operation. Statistics reported by Boeing (2018) show that 322 non-fatal and 51 fatal accidents occurred worldwide in commercial jet flights from 2009 through 2018. Of the fatal accidents, the largest proportion (25.5%) were due to Loss of Control-In Flight (LOC-I). The International Air Transportation Association (2016) shows that LOC-I frequently occurs when the aircraft speed is well below the stall speed; in conjunction with weather conditions, low speed is the most common factor in LOC-I accidents. Forty-two percent of LOC-I accidents occurred under

degraded meteorological conditions affecting aircraft speed, in particular strong wind shear and atmospheric turbulence.

For both fatal and non-fatal aircraft accidents, the impact of atmospheric turbulence can be significant. The Japan Transport Safety Board has stated that accidents caused by turbulence accounted for 48% of non-fatal aircraft accidents in Japan involving commercial airplanes from 2003-2012. An increase in the rate of accidents related to turbulence was reported by the Federal Aviation Administration in 2006, Kim and Chun in 2011, and Williams in 2017.

d) Line 38: There are numerical predictions of CAT. Please add a statement and provide any supporting references for if/why these are insufficient for avoiding CAT.

We have modified the manuscript as follows:

Numerical weather prediction (NWP), which is an essential tool for aircraft operation, can forecast weather conditions for days and even weeks in advance and output broader-area weather information than can Radar or Lidar. However, NWP cannot explicitly resolve disturbances as small as most turbulence, leading to a very large predictive uncertainty (Sharman et al. 2006, Kim et al. 2011). Therefore, some researchers have developed an alternative approach that predicts turbulence potential by calculating turbulence indicators from NWP results; for example, Sharman et al. (2006) have developed an approach called graphical turbulence guidance (GTG) that combines such indicators. The turbulence potential can also be used to determine operational flight routes (Kim et al. 2015), but it has a large spatio-temporal gap on the scale of aircraft motion because it is based on NWP results such as the meso-scale model. It thus provides insufficient information to implement turbulence avoidance on aircraft in flight.

e) Line 42: Rephrase the sentence ‘Aerosol particles are received instead of laser beams due to a scattering light effect caused by the rain particles’, as it is unclear. Does this mean that the dominant signal comes from raindrops, which are not passive tracers of air motion (whereas aerosols can be safely assumed to be passive tracers due to their small size).

We have modified the manuscript as follows:

Emitted laser light is scattered by fine aerosol particles in the atmosphere; the back-scattered light is condensed by telescopes and received by an optical transceiver. Since the wavelength of the received light varies according to the velocity of the aerosol particles due to the Doppler effect, wind speed can be calculated by comparing this wavelength with that of the received light (Inokuchi and Akiyama, 2019). However, when rain is too heavy, the backscattering signal is weakened due to strong

attenuation by raindrops and a decrease in aerosols (Wei et. al 2019), making it difficult to measure the wind velocity at a distance.

f) Line 48: How far in front of an aircraft can CAT be detected?

We have modified the manuscript as follows:

Inokuchi et al. (2012) have shown observationally that airborne Doppler Lidar can detect CAT in front of an aircraft in flight at altitudes of 3,200 m; the Lidar information can be detected 30 seconds before the turbulence affects the aircraft. The aircraft's flight speed in the test was 320 kt (160 m/s), so it detected CAT from a distance of about 4.8 km.

g) Line 75: This is not true. A single lidar can measure the vertical velocity if the beam is scanned at different angles (e.g., upwards and downwards using a prism). It is only not possible when the beam is fixed.

We have modified the manuscript as follows:

However, a fixed single Doppler Lidar system can only detect the line-of-sight (LOS) wind, providing a one-dimensional piece of information; the vertical wind velocity in front of the aircraft cannot be measured by such a system (Hamada, 2019). It is necessary to perform the Lidar measurements in two directions, upward and downward, to obtain the vertical wind velocity (Neininger, 2017).

h) Line 92: Clarify there and throughout that the horizontal wind (u and v) is not measured, rather only the component that is parallel to the look-direction (i.e., headwind/tailwind component, not crosswind).

We have modified the manuscript as follows:

In this study, "horizontal wind" means any headwind/tailwind component that does not include the crosswind component.

i) Sect. 2.1: Please provide more details on the Doppler lidar itself. Does it use heterodyne- or direct-detection? What is its wavelength, PRF, pulse energy, band-width, aperture diameter, etc? How many pulses are averaged? What is the data rate? Also list any other relevant details and provide a written description of the system.

We have modified the manuscript as follows:

The Lidar sensor is shown in Fig. 2; its specifications are given in Table 1 (Inokuchi and Akiyama 2019). Laser pulses generated by an optical transceiver are amplified by optical amplifiers (Sakimura et. al. 2013) incorporated into an optical antenna and radiated into the atmosphere from optical telescopes. The heat generated by the optical amplifiers is dissipated by a water-cooled chiller unit. The optical antenna is equipped with a 150 mm large-aperture telescope for long range observations and a 50 mm small-aperture telescope for vector conversion of short-range observations.

j) Line 120: Where do these requirements for the frequency/accuracy come from?

We have modified the manuscript as follows:

The control requirements are the conditions necessary to halve the peak variation in acceleration by control. This value has been specified using control simulations (Hamada, 2019), and Monte Carlo simulations have also been performed.

k) Line 131: Change 'areas' to 'distance', as area connotes a 2-D space. Also change the wording 'area' in Fig.2.

We modified the Figure 2 (Figure 3 in revised paper) according to the referee's comment. See answer to (l) below.

l) Figure 2: The circles in the figure make it seem like the lidars are sweeping out a scan circle (similar to a conical scan). This is not true, suggest removing the circles.

We have modified Fig. 2 (now Fig. 3) as follows:

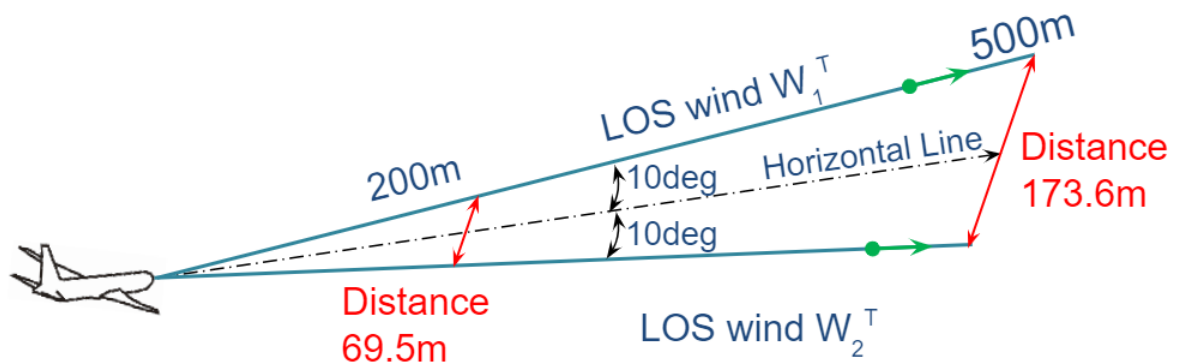


Fig. 3 Distance to wind-field region between the Lidars for two line-of-sight (LOS) distances

m) Line 156: Why was a first-degree polynomial used and not a higher-order polynomial?

We have modified the manuscript as follows:

Depending on the number of past LOS wind data used, the order of the polynomial expression used in the extrapolation varies. The aerosol concentration in the upper sky is low, suggesting that there is considerable missing data and noise. A sufficient number of past LOS wind data may not be available to estimate a high-order polynomial expression, and this could affect the robustness of the control. For this reason, a first-degree polynomial expression is adopted in this study and used in the least-squares method (LSM) to extrapolate the wind-field values according at the horizontal line. The airflow vector is calculated by Eq. (1) using the extrapolated LOS wind.

n) Sect. 2.3: It would be helpful if a figure could be added showing one more multiple example spectra (preferably for both a valid and invalid measurement), also showing what these values (k_{1st} , k_{2nd} , k_{ave}) signify.

We have modified the manuscript as follows:

Figure 5 shows a conceptual explanation of the variables of simplified Kalman gain in the cases of correct measurement and of an error peak. In this study, the filtering algorithm is carried out first when the observation data is obtained:

$$K = \begin{cases} 1 & |k_{1st} - k_{2nd}| = 1 \text{ and } |k_{1st} - k_{ave}| < k_{dif} \\ 0 & \text{Otherwise} \end{cases} \quad (4)$$

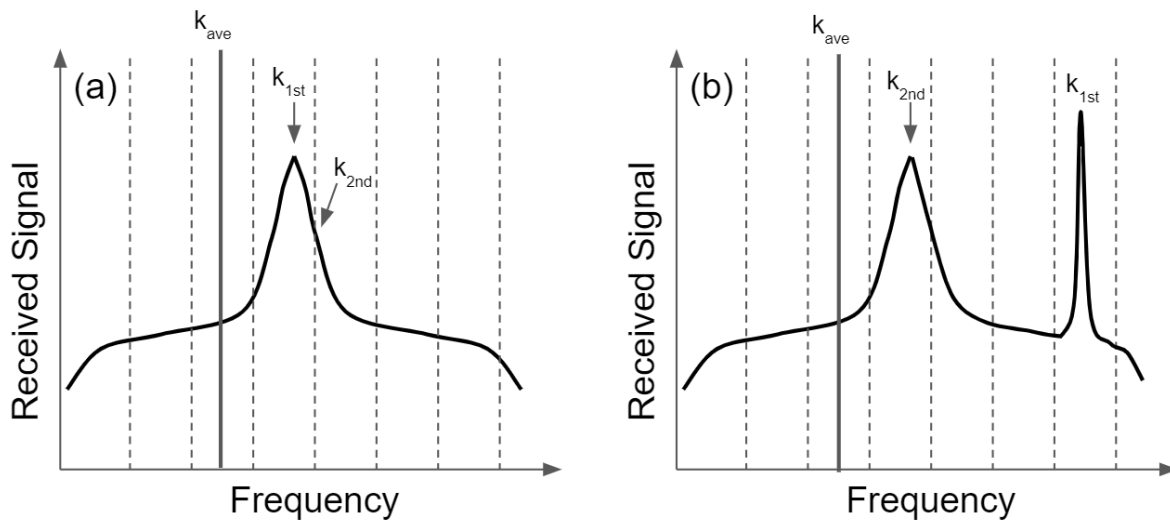


Fig. 5 Conceptual explanation of the variables of simplified Kalman gain.

(a) Correct measurement case of $K=1$. (b) Case with the error peak of $K=0$

o) Lines 175-189: It would also be help to add a figure showing how exactly the LSM estimation is used to QC bad measurements. Once invalid measurements are removed following this LSM quality-control process, is the initial LSM fitting done again to obtain a better estimate of the wind? I would think this process could be repeated until there

are no more poor LOS estimates going into the fitting.

We have added a figure, as the referee suggested, and modified the manuscript as follows:

Figure 6 explains the concept behind Tuckey's biweight methodology as applied to Lidar. The concept of a robust LSM is validated by analyzing the difference between the observed LOS wind values and those estimated by the polynomial expression used in LSM. In the 1st step, the LOS wind is estimated by using the general LSM (Eq. (2)). In the 2nd step, the difference d_j^T between the observed LOS wind value and that estimated from the polynomial expression is found:

$$d_j^T = W_j^T - (a_j z + b_j). \quad (5)$$

A permissible difference range L is defined and weights $w_j^T(d_j^T)$ are calculated depending on where d_j^T falls in the distance range:

$$\begin{aligned} w_j^T(d_j^T) &= 0 \quad (d_j^T < -L) \\ w_j^T(d_j^T) &= \left(1 - \left(\frac{d_j^T}{w_j^T}\right)^2\right)^2 \quad (-L \leq d_j^T \leq L) . \\ w_j^T(d_j^T) &= 0 \quad (d_j^T > L) \end{aligned} \quad (6)$$

Weights are assigned to each LOS wind velocity value. In the 3rd step, a new first-degree polynomial expression for the LSM with the weighted data is estimated as follows.

$$\begin{aligned} a_j' &= \frac{\sum_{i=T-(N-1)}^T w_j^i \sum_{i=T-(N-1)}^T w_j^i z^i W_j^i - \sum_{i=T-(N-1)}^T w_j^i z^i \sum_{i=T-(N-1)}^T w_j^i W_j^i}{\sum_{i=T-(N-1)}^T w_j^i \sum_{i=T-(N-1)}^T w_j^i (z^i)^2 - \left(\sum_{i=T-(N-1)}^T w_j^i z^i\right)^2} \\ b_j' &= \frac{\sum_{i=T-(N-1)}^T w_j^i \sum_{i=T-(N-1)}^T w_j^i W_j^i - \sum_{i=T-(N-1)}^T w_j^i z^i \sum_{i=T-(N-1)}^T w_j^i W_j^i}{\sum_{i=T-(N-1)}^T w_j^i \sum_{i=T-(N-1)}^T w_j^i (z^i)^2 - \left(\sum_{i=T-(N-1)}^T w_j^i z^i\right)^2} \end{aligned} \quad (7)$$

This process is repeated until the weight of the error value decreases and converges.

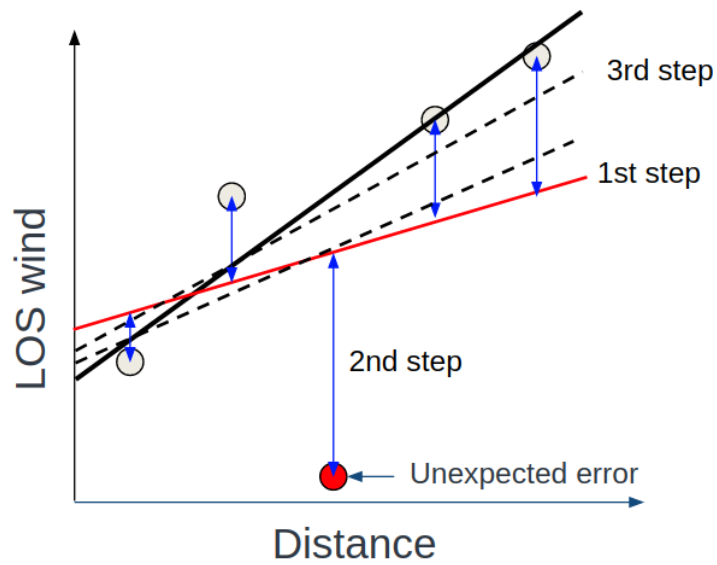
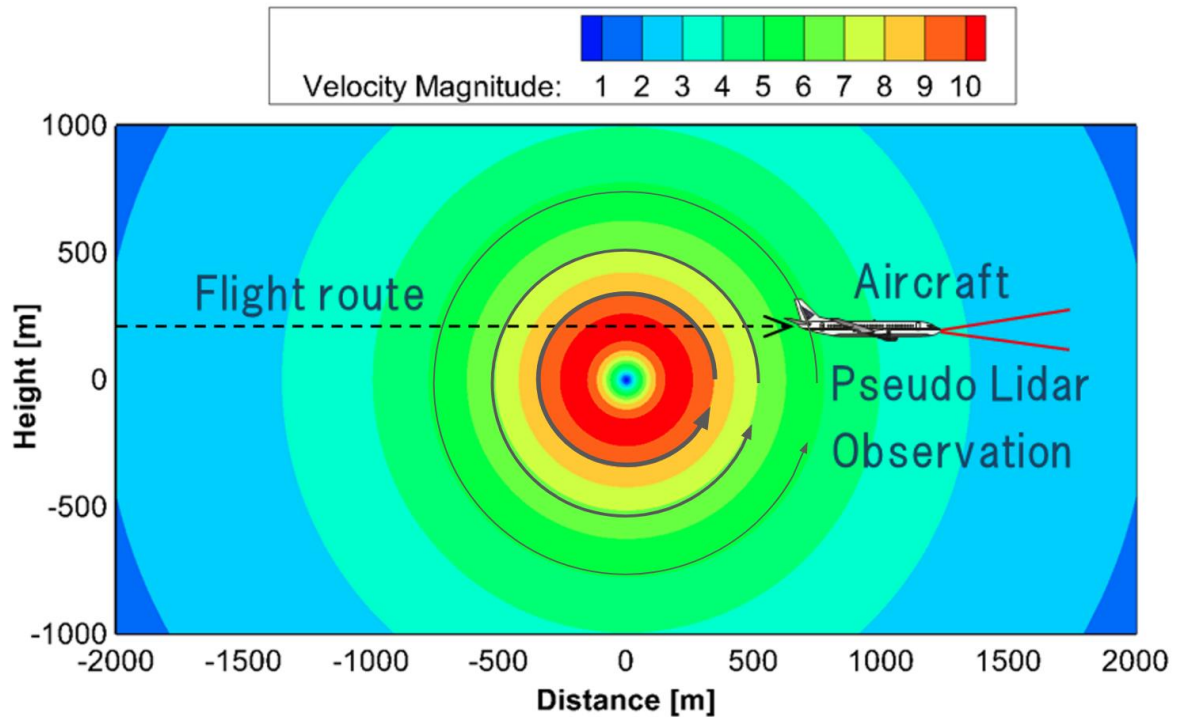


Fig. 6 Conceptual explanation of Tuckey's biweight methodology applied to line-of-sight (LOS) wind at various distances. First step: simple least-squares fit. Second step: observations are compared with the estimate. The data are weighted, and extreme outliers are excluded, using Eq. (6). Third step: Least-squares fit of the weighted data.

p) Figure 5: It makes sense to show the vertical velocity with its sign, not just it's magnitude, in this plot, as the sign is expected to change around the vortex.

We modified the Figure 5 (Figure 8 in revised paper) according to the referee's comment. As the referee comments, it is important to specify the direction of rotation of a vortex because the vertical wind speed changes from positive to negative around the vortex. Therefore, the direction of rotation of the vortex is now indicated by arrows in the revised figure.



q) Figure 6: I don't really think this figure is valuable and it could be removed. The only information it contains that is not in the text is the dimensions of the model volume, which could be stated in the text instead.

Figure 6 has been removed, in agreement with the referee's comment.

r) Figure 7: I suggest using a divergent colorbar (i.e., a colorbar that is either white or grey for $w=0$), which is typically used for vertical velocity. It would be helpful to add the modeled flight path to this figure.

We modified Figure7 (Figure 9 in revised paper) according to the referee's comment. Because of the difference in the maximum and minimum vertical winds at the top and bottom and the difficulty of setting the divergent colorbar center to 0 m/s, the colorbar was left as it was. However, an example of an aircraft flight path is shown.

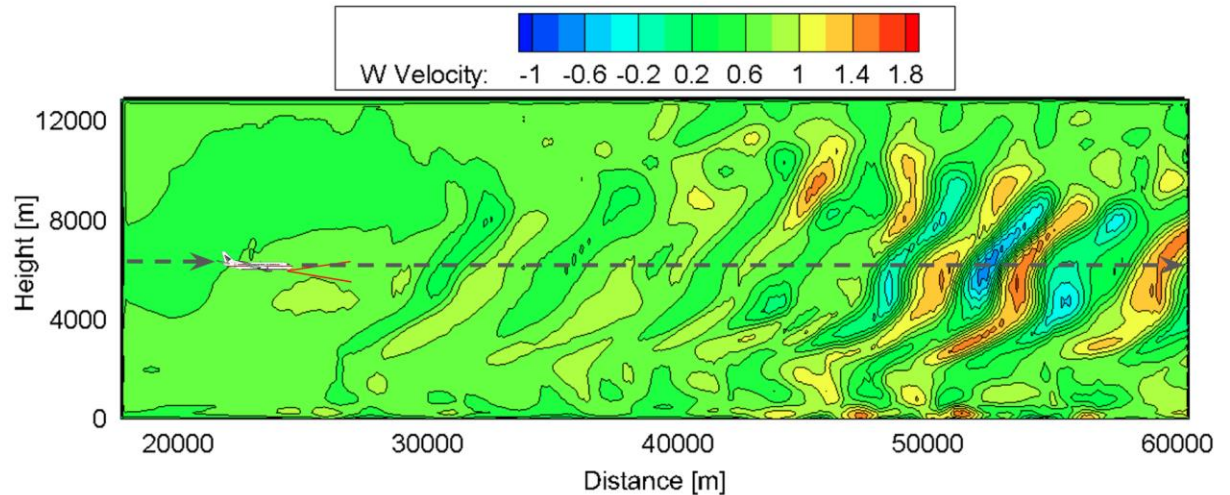


Fig. 9 Vertical wind velocity distribution map generated by JMA-NHM

s) Lines: 271-275: These lines would be best in the caption for Figs. 9 and 10, that way the reader doesn't need to refer back (several pages in the text) to understand what is in Fig. 9 and 10 when examining those figures.

We have modified the manuscript as follows (note that Fig. 9 is now Fig. 11):

Fig. 11 Distributions of the horizontal and vertical wind components estimated by the simple vector conversion method vs. the proposed method (at time 10 s). Upper figures: ideal vortex model; middle figures: simple vector conversion method; lower figures: proposed method with five-past LOS wind datasets. Left figures: horizontal wind values; right figures: vertical wind values

and a similar for Fig. 12 (at time 15 sec).

t) Line 275: Clarify what is meant exactly by 'after 10 s or 15 s'?

We have modified the manuscript as follows:

Figures 11 and 12 show the results of starting the flight from the edge of the computational space, 10 and 15 seconds later and 15 seconds later. Thus, they represent the time before and during the aircraft's close approach to the vortex core.

u) Line 301 and 331, 389: How are the pseudo-routes generated? Are they at random locations in the vortex, or staggered? Are there limits to the heights that they are limited to?

We have modified the manuscript as follows:

Line 353: Next, the statistical estimation performance is evaluated by using 100 pseudo-routes that are randomly generated 750 m up and down from the center of the vortex core.

Line 386: Next, the statistical estimation performance is evaluated using 100 pseudo-routes that are randomly generated between 2 km and 10 km altitude.

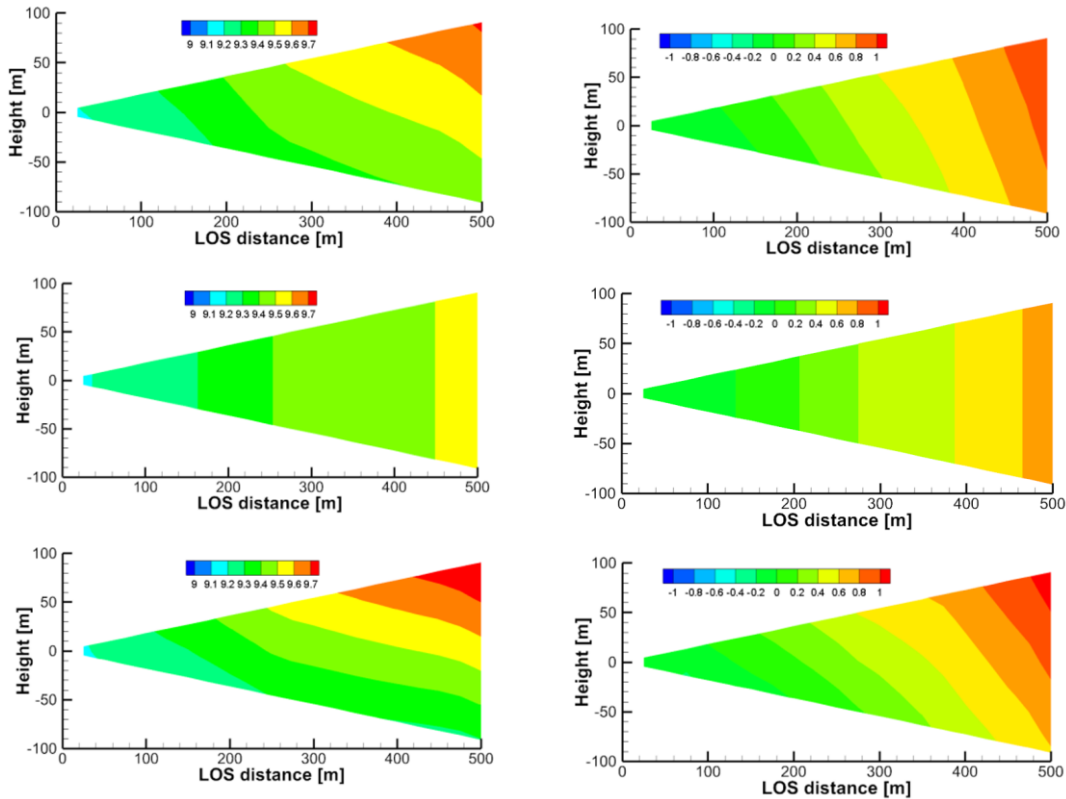
Line 418: Next, the statistical estimation performance [in this case, different from that in Line 353] is evaluated by using 100 pseudo-routes that are randomly generated 750 m up and down from the center of the vortex core.

v) Lines 322-325: These lines also would be best in the caption for Figs. 11 and 12.

We modified the sentences and added the explanation to the caption according to the referee's comment.

w) Fig. 12: The colorbar axis on the right plots is not correct. It shows vertical winds of 8 m/s, but the values shown for the NWP output (Fig. 7) did not exceed 2 m/s.

The right colorbar of Fig. 12 (now called Fig. 14) was indeed incorrect and has been modified:



x) Lines 391-392: This text should be moved to the caption to describe what each

panel indicates.

We modified the sentences and added the explanation to the caption according to the referee's comment.

y) Line 425: One notable exception to this is wakes from other (larger) aircrafts. These localized but intense vortices pose a safety hazard. The authors should specifically state here that these hazards will not be detected with this technique.

We have modified the manuscript as follows:

An exception to this is aircraft-generated wake turbulence, which still poses a safety risk. The radius of the actively fluctuating wake-turbulence core is only a few meters, so the proposed method could lead to erroneous predictions.

Editorial Corrections

a) Line 87: Change 'smaller than that in the atmosphere' to 'smaller than at lower altitudes'.

We have modified the manuscript as follows:

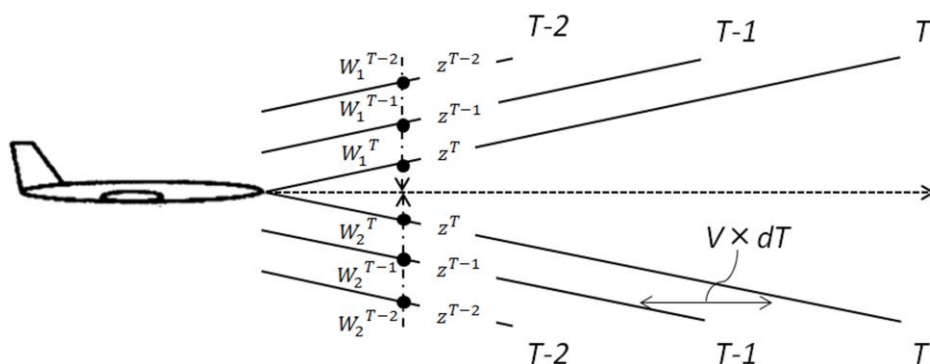
In addition, actual Lidar observations involve errors, noise, and loss of data, with negative effects on aircraft control, as reported by Misaka et al. (2015); these problems are worse at higher altitudes, where the aerosol density is smaller than it is at lower ones.

b) Line 151: Remove one instance of the word 'method'.

We have modified the sentence according to the referee's comment.

c) Figure 3: The top-middle lidar beam should be labeled T-1, not T-2.

We have modified the manuscript as follows:



1 Real-Time Estimation of Airflow Vector based on Lidar 2 Observations for Preview Control

3 Ryota Kikuchi^{1,2}, Takashi Misaka³, Shigeru Obayashi⁴, Hamaki Inokuchi²
4

5 ¹DoerResearch Inc., Chiba 260-0013, Japan

6 ²Japan Aerospace Exploration Agency, Tokyo 181-0015, Japan

7 ³National Institute of Advanced Industrial Science and Technology, Ibaraki 305-8564, Japan

8 ⁴Tohoku University, Miyagi 980-8577, Japan
9

10 *Correspondence to:* Ryota Kikuchi (Email: kikuchi-ryota@doerresearch.com)

11 **Abstract.** As part of control techniques, gust-alleviation systems using airborne Doppler Lidar technology are
12 expected to enhance aviation safety by significantly reducing the risk of turbulence-related accidents. Accurate
13 measurement and estimation of the vertical wind velocity are very important in the successful implementation of such
14 systems. An estimation algorithm for the airflow vector based on data from airborne Lidars is proposed and
15 investigated for preview control to prevent turbulence-induced aircraft accidents in flight. An existing technique —
16 simple vector conversion— assumes that the wind field between the Lidars is homogeneous, but this assumption fails
17 when turbulence occurs due to a large wind-velocity fluctuation. The proposed algorithm stores the line-of-sight (LOS)
18 wind data at every moment and uses recent and past LOS wind data to estimate the airflow vector and to extrapolate
19 the wind field between the airborne twin Lidars without the assumption of homogeneity. Two numerical
20 experiments—using the ideal vortex model and numerical weather prediction, respectively—were conducted to
21 evaluate the estimation performance of the proposed method. The proposed method has much better performance than
22 simple vector conversion in both experiments, and it can estimate accurate two-dimensional wind-field distributions,
23 unlike simple vector conversion. The estimation performance and the computational cost of the proposed method can
24 satisfy the performance demand for preview control.

25 1 Introduction

26 Atmospheric turbulence poses a potential risk to aircraft operation. Statistics reported by Boeing (2018) show
27 that 322 non-fatal and 51 fatal accidents occurred worldwide in commercial jet flights from 2009 through 2018. Of
28 the fatal accidents, the largest proportion (25.5%) were due to Loss of Control-In Flight (LOC-I). The International
29 Air Transportation Association (2016) shows that LOC-I frequently occurs when the aircraft speed is well below the
30 stall speed; in conjunction with weather conditions, low speed is the most common factor in LOC-I accidents. Forty-
31 two percent of LOC-I accidents occurred under degraded meteorological conditions affecting aircraft speed, in
32 particular strong wind shear and atmospheric turbulence.

33 For both fatal and non-fatal aircraft accidents, the impact of atmospheric turbulence can be significant. The
34 Japan Transport Safety Board has stated that accidents caused by turbulence accounted for 48% of non-fatal aircraft
35 accidents in Japan involving commercial airplanes from 2003-2012. An increase in the rate of accidents related to
36 turbulence was reported by the Federal Aviation Administration in 2006, Kim and Chun in 2011, and Williams in
37 2017. Accidents caused by convective systems such as cumulonimbus clouds have decreased owing to advances in
38 airborne Radar (Airbus, 2020; Sermi et al. 2015). However, non-cloud atmospheric turbulence, called clear-air
39 turbulence (CAT), cannot be detected by Radar, as reported by Soreide et al., 2000; Barny, 2012; and Inokuchi et al.,
40 2009. Airborne CAT-observation systems to minimize risks of turbulence-related accidents are essential for aviation
41 safety.

42 Numerical weather prediction (NWP), which is an essential tool for aircraft operation, can forecast weather
43 conditions for days and even weeks in advance and output broader-area weather information than can Radar or Lidar.
44 However, NWP cannot explicitly resolve disturbances as small as most turbulence, leading to a very large predictive
45 uncertainty (Sharman et al. 2006, Kim et al. 2011). Therefore, some researchers have developed an alternative
46 approach that predicts turbulence potential by calculating turbulence indicators from NWP results; for example,
47 Sharman et al. (2006) have developed an approach called graphical turbulence guidance (GTG) that combines such
48 indicators. The turbulence potential can also be used to determine operational flight routes (Kim et al. 2015), but it
49 has a large spatio-temporal gap on the scale of aircraft motion because it is based on NWP results such as the meso-
50 scale model. It thus provides insufficient information to implement turbulence avoidance on aircraft in flight.

51 Recently, airborne Doppler Lidar has been developed by Soreide et al., 2000; Barny, 2012; Inokuchi et al.,
52 2009; Machida, 2017; and Inokuchi and Akiyama, 2019. Emitted laser light is scattered by fine aerosol particles in
53 the atmosphere; the back-scattered light is condensed by telescopes and received by an optical transceiver. Since the
54 wavelength of the received light varies according to the velocity of the aerosol particles due to the Doppler effect,
55 wind speed can be calculated by comparing this wavelength with that of the received light (Inokuchi and Akiyama,
56 2019). However, when rain is too heavy, the backscattering signal is weakened due to strong attenuation by raindrops
57 and a decrease in aerosols (Wei et. al 2019), making it difficult to measure the wind velocity at a distance. Japan
58 Aerospace Exploration Agency (JAXA) is researching and developing a coherent Doppler Lidar capable of remotely
59 detecting air turbulence in clear-air conditions, and has conducted a flight demonstration of a Lidar system that can
60 provide turbulence information to pilots (Inokuchi et al., 2009; Machida, 2017; Inokuchi and Akiyama, 2019).
61 Inokuchi et al. (2012) have shown observationally that airborne Doppler Lidar can detect CAT in front of an aircraft
62 in flight at altitudes of 3,200 m; the Lidar information can be detected 30 seconds before the turbulence affects the
63 aircraft. The aircraft's flight speed in the test was 320 kt (160 m/s), so it detected CAT from a distance of about 4.8
64 km.

65
66
67 Based on advance airflow information, flight demonstrations have been carried out with the aim of providing pilots
68 with the information they need to make decisions: whether to change course to avoid wind shear, and whether to turn
69 on seatbelt-sign lighting during cruise and altitude changes (Inokuchi and Akiyama, 2019). Although Lidar systems

70 are useful for providing onboard wind information to pilots, avoiding turbulence at high altitudes is difficult as the
71 range of detection that facilitates pilots to be warned is short (Hamada, 2019). Gathering such information involves
72 emitting a laser beam and receiving the scattered light from aerosol particles that are much smaller than precipitation
73 droplets in the air. Therefore, when the number of aerosol particles that emit scattered light is small, it is difficult to
74 measure wind information at a distance. Furthermore, as altitude increases, the aerosol density decreases, and the
75 observation range tends to decrease accordingly. The maximum observation range and aerosol density measured at
76 each altitude are shown in Inokuchi and Akiyama, 2019.

77 Advance knowledge of turbulent atmospheric conditions would improve the performance of automatic
78 aircraft-vibration reduction systems. Automatic control to alleviate aircraft vibration is called gust-alleviation and has
79 been studied since the 1970s, mostly with only the help of feedback sensors such as inertial measurement units (Regan
80 and Jutte, 2012). Recently, methods of reducing the vibrations due to turbulence with the help of preview controlling
81 based on airborne Lidar observation have been reported by Schmitt et al., 2007; Fezans et al., 2019; and Hamada,
82 2019. The aim of the Aircraft Wing with Advanced Technology Operation (AWIATOR) project is the development
83 of new direct-lift control devices and a Lidar system for turbulence measurement (Schmitt et al., 2007). Another
84 project—“Demonstration of Lidar-based CAT detection” (DELICAT) (Barny, 2012)—developed airborne ultraviolet
85 Lidar for gust and turbulence measurements. The test flights were carried out using an Airbus 340 aircraft equipped
86 with ultraviolet Lidar. In both the AWIATOR and the DELICAT experiments, the measurement range was short,
87 because the Lidar was developed for controlling the aircraft automatically.

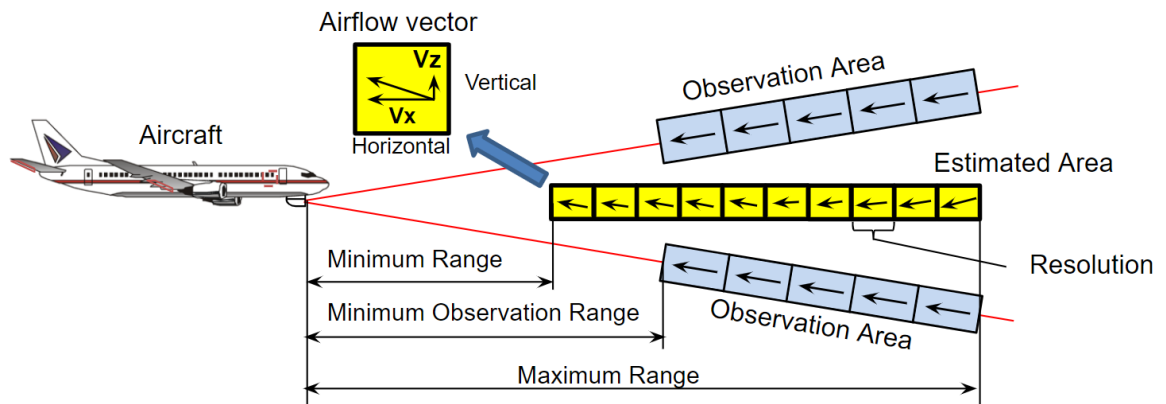
88 In order to implement an airborne Doppler Lidar gust-alleviation system successfully, it is very important to
89 measure the vertical wind velocity accurately. Both horizontal and vertical winds affect aircraft motion, but the effect
90 of changing the vertical wind velocity is greater. This is because the effect of modifying the angle of attack is relatively
91 larger than the effect of changing the horizontal wind velocity, which affects only the airspeed (Fezans et al., 2019).
92 However, a fixed single Doppler Lidar system can only detect the line-of-sight (LOS) wind, providing a one-
93 dimensional piece of information; the vertical wind velocity in front of the aircraft cannot be measured by such a
94 system (Hamada, 2019). It is necessary to perform the Lidar measurements in two directions, upward and downward,
95 to obtain the vertical wind velocity (Neininger, 2017). Figure 1 shows a representation of this concept. The vertical
96 wind-velocity vector is generated from the differences between the upward and downward LOS winds by using simple
97 vector conversion. Unfortunately, this method is incapable of estimating the vertical wind velocity with high accuracy
98 to control the aircraft automatically because the technique assumes homogeneity between the upward and downward
99 Lidars (Fezans et al., 2019). In this study, a fully turbulent field with atmospheric turbulence and gusts is considered;
100 under these conditions, it is difficult to estimate the vertical wind velocity with high accuracy using simple vector
101 conversion. In particular, the estimation accuracy of the vertical wind velocity rapidly worsens when the estimation
102 position is located farther ahead from the aircraft.

103 In addition, actual Lidar observations involve errors, noise, and loss of data, with negative effects on aircraft
104 control, as reported by Misaka et al. (2015); these problems are worse at higher altitudes, where the aerosol density is
105 smaller than it is at lower ones. Misaka et al. (2015) proposed a filtering algorithm based on a simple Kalman filter to
106 remove wind-velocity errors from Lidar measurements. For preview control, it is essential to deal with the Lidar errors,

107 noise and loss of data more carefully. An accurate airflow vector estimation method and an efficient real-time filtering
108 algorithm are required.

109 In this study, an estimation method and an airflow-vector filtering algorithm are proposed for preview control
110 to prevent turbulence-induced aircraft accidents. The method works for both horizontally and vertically directed winds,
111 and uses both upward and downward Lidars. (In this study, “horizontal wind” means any headwind/tailwind
112 component that does not include the crosswind component.) The Lidar system in this paper is that also used by JAXA
113 in its ongoing “Lidar-based gust alleviation control” research project. The Lidars are assumed to be compliant with
114 the specifications for preview control currently under development by the JAXA. The proposed algorithm stores the
115 LOS wind data continually and uses recent and past LOS wind data to estimate the airflow vector and the wind field
116 between Lidars, whereas simple vector conversion utilizes only recent LOS wind data. The airflow vector is calculated
117 by using wind data extrapolated from the horizontal and vertical wind components; the estimation accuracy of the
118 airflow vector in front of the aircraft is improved by using such extrapolated wind data because the region between
119 the Lidars represents a non-homogeneous one. A polynomial expression is used to extrapolate the wind field. In
120 addition, the proposed method can estimate the two-dimensional distribution of the wind field between the Lidars,
121 which simple vector conversion cannot.

122 Two test configurations—an ideal vortex flow field and a weather field—are calculated by an NWP system
123 and utilized to evaluate the performance of the airflow vector. These experiments generate a large number of pseudo-
124 Lidar measurements along flight routes from the reference wind field for evaluation of the estimated performance.
125 Comparing the prediction results with the reference wind field can confirm all the wind-field values.



126

127

Fig. 1 Concept of the airborne Lidars observation system

128 2 Methods

129

2.1 Airborne Lidar Specifications

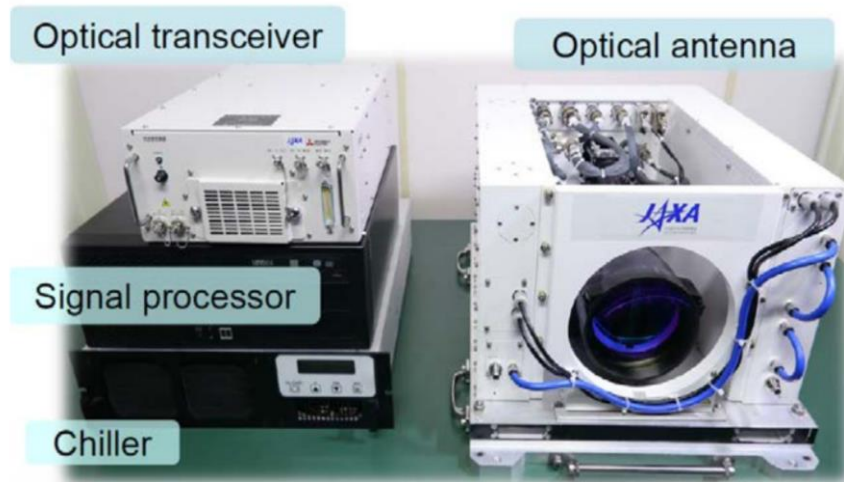
130

131

132

The airborne Lidar observation system currently under development by JAXA for preview control to prevent turbulence-induced aircraft accidents is shown in this section. This system has airborne Lidars that are aiming upwards and downwards; the angle between them is 20 degrees, that is, 10 degrees between the horizontal line and each Lidar.

133 The Lidar sensor is shown in Fig. 2; its specifications are given in Table 1 (Inokuchi and Akiyama 2019). Laser pulses
 134 generated by an optical transceiver are amplified by optical amplifiers (Sakimura et. al. 2013) incorporated into an
 135 optical antenna and radiated into the atmosphere from optical telescopes. The heat generated by the optical amplifiers
 136 is dissipated by a water-cooled chiller unit. The optical antenna is equipped with a 150 mm large-aperture telescope
 137 for long range observations and a 50 mm small-aperture telescope for vector conversion of short-range observations.
 138 Each Lidar measures the LOS wind velocity with an observational accuracy of $\pm .09 \text{ m s}^{-1}$; the paired values are used
 139 to estimate the airflow vector in the region between the Lidars. The observational resolution of each Lidar is
 140 approximately 25 m. There are additional performance requirements for preview control: the estimation frequency
 141 and estimation accuracy of vertical wind velocity. The frequency of estimation must be more than 5 Hz, and the
 142 estimation accuracy of the vertical wind velocity must be better than 2.6 m s^{-1} in the LOS distance of 500 m. The
 143 control requirements are the conditions that are necessary for halving the peak variation in acceleration by control.
 144 This value has been specified using control simulations (Hamada, 2019), and Monte Carlo simulations have also been
 145 performed.



146
 147 **Fig. 2 Coherent Doppler Lidar used in this work**
 148

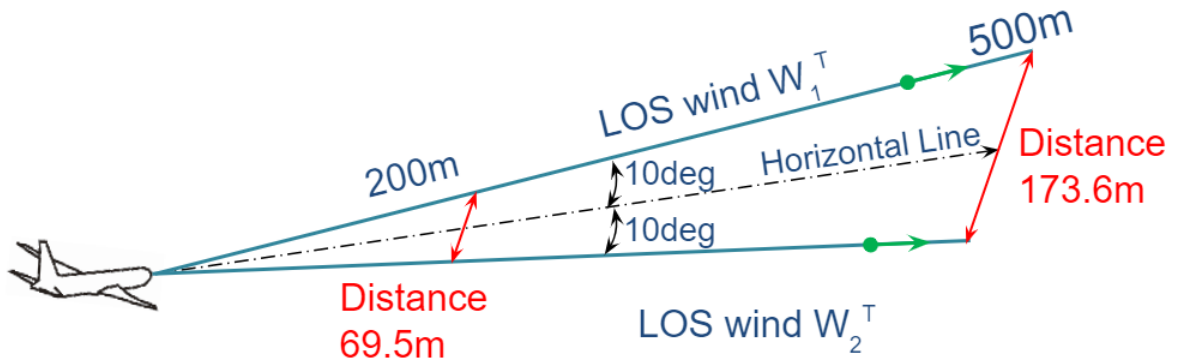
149 **Table 1. Coherent Doppler Lidar Specifications**

Laser Wavelength	1.55 μm
Laser Output	3.3 W
Pulse Repetition Frequency	1,000 Hz
Laser Beam Diameter	150, 50 mm
System Weight	83.7 kg
Power Consumption	936 W
Data Rate	5 Hz

150 Next, an existing technique for estimating the airflow vector from a pair of LOS wind values is reviewed.
 151 The airflow vector in the region between the upward and downward Lidars is conventionally estimated via simple
 152 vector conversion. This procedure is similar in concept to the vertical azimuth display approach used in general ground
 153 Lidar systems (Newsom et al., 2017). The simple vector conversion is given by

$$\begin{aligned} u_x^T &= \frac{(W_1^T + W_2^T)}{2\cos\theta}, \\ u_z^T &= \frac{(W_1^T - W_2^T)}{2\sin\theta}, \end{aligned} \quad (1)$$

154 where u_x^T and u_z^T are the horizontal and vertical wind velocity measurements at the observation time T ; W_1^T and
 155 W_2^T are the LOS wind velocities of the upward and downward directed Lidars at the observation time T ; and θ is the
 156 angle between the horizontal line and each Lidar, which is 10 degrees in this study. The simple vector conversion
 157 assumes that the wind-field region between the Lidars is homogeneous (Newsom et al., 2017). The assumption of
 158 homogeneity seems natural: the regions between the Lidars are 69.5 m and 173.6 m at the LOS distances of 200 m
 159 and 500 m ahead of the aircraft (Fig. 3). Nevertheless, the assumption would be wrong if a large fluctuation in wind
 160 velocity occurs, creating turbulence. In homogenous conditions, a simple vector conversion can estimate the airflow
 161 vector accurately; however, in non-homogenous conditions, the estimation is expected to have poor accuracy.



162
 163 **Fig. 3 Distance to wind-field region between the Lidars for two line-of-sight (LOS) distances**

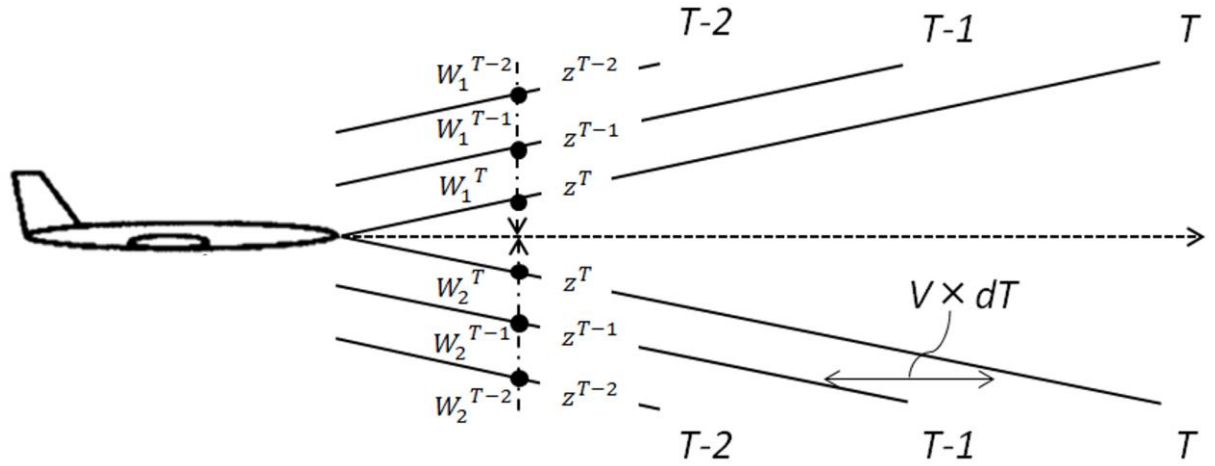
164 2.2 Estimation Algorithm Based on Extrapolation

165 Whereas simple vector conversion utilizes recent LOS wind data to estimate the airflow vector, our proposed
 166 method stores the LOS wind data continuously and uses both recent and past values to extrapolate the wind field in
 167 the region between the Lidars where it has not been directly measured. The airflow vector is then calculated from Eq.
 168 (1) and the extrapolated horizontal and vertical components of the wind velocity. The airflow-vector estimation
 169 accuracy far ahead of the aircraft is improved relative to simple vector conversion by using the extrapolated wind data
 170 because the region between the upward and downward Lidars is no longer assumed to be homogeneous; our algorithm
 171 uses a polynomial expression to extrapolate data points from both recent and past measurements, allowing it to be

172 used in non-homogenous wind fields. In addition, the proposed method can estimate the two-dimensional distribution
 173 of the wind field between the Lidars, again unlike simple vector conversion.

174

175 Figure 4 shows the overview of the proposed estimation method when a current data point and two past data
 176 points are used. When the aircraft speed is V and the time span of observation is dt , the airflow moves backwards at
 177 $V \times dt$ because the aircraft is advancing. Current observation times are denoted as T and past observation times as $T-1$
 178 and $T-2$. The proposed method uses the current LOS wind values (W_1^T and W_2^T) and the past LOS wind values (W_1^{T-1} , W_2^{T-1}
 179 and W_1^{T-2} , W_2^{T-2}). The perpendicular distances between the horizontal line and each Lidar are denoted as z^T ,
 180 z^{T-1} , and z^{T-2} , respectively. Depending on the number of past LOS wind data used, the order of the polynomial
 181 expression used in the extrapolation varies. The aerosol concentration in the upper sky is low, suggesting that there is
 182 considerable missing data and noise. A sufficient number of past LOS wind data may not be available to estimate a
 183 high-order polynomial expression, and this could affect the robustness of the control. For this reason, a first-degree
 184 polynomial expression is adopted in this study and used in the least-squares method (LSM) to extrapolate the wind-
 185 field values according at the horizontal line. The airflow vector is calculated by Eq. (1) using the extrapolated LOS
 186 wind. The equation used in the extrapolation method is



187

188 **Fig. 4 Overview of estimation by proposed method when line-of-sight wind data from 0, 1, and 2 past time-steps dT**
 189 **are used. V = speed of aircraft; W_1^T and W_2^T = wind speeds measured at time T by the two Lidars; z = vertical distance**
 190 **perpendicular to velocity of aircraft**

191

$$W_j'(z) = a_j z + b_j, \quad (2)$$

where

$$a_j = \frac{N \sum_{i=T-(N-1)}^T z^i W_j^i - \sum_{i=T-(N-1)}^T z^i \sum_{i=T-(N-1)}^T W_j^i}{N \sum_{i=T-(N-1)}^T (z^i)^2 - \left(\sum_{i=T-(N-1)}^T z^i \right)^2}, \quad (3)$$

$$b_j = \frac{\sum_{i=T-(N-1)}^T z^i \sum_{i=T-(N-1)}^T W_j^i - \sum_{i=T-(N-1)}^T W_j^i \sum_{i=T-(N-1)}^T z^i}{N \sum_{i=T-(N-1)}^T (z^i)^2 - \left(\sum_{i=T-(N-1)}^T z^i \right)^2}.$$

192

193

2.3 Filtering Error and the Lack of Wind-Velocity Data

194

195

196

197

198

199

200

201

202

203

204

205

206

207

In this study, two filtering algorithms are used to remove the error and the loss of data in airborne Lidars. First, a filtering algorithm that is a simple representation of a Kalman filter with simplified Kalman gain is used; **this filtering algorithm is described in detail in the study of Misaka et al., 2015.** The algorithm assumes that infinite variance is used to exclude outliers and loss of data. This method uses the Lidar spectrum data at each range-bin; the algorithm defines the validity of the measurements during the Lidar data peak-detection process. To identify the correct and incorrect LOS wind-velocity values, two spectrum thresholds are defined. First, the largest and second-largest spectrum values, k_{1st} and k_{2nd} , which are the Fast Fourier Transform points for the first and second spectrum peaks, respectively, are adjacent to each other; i.e., the magnitude of the distance between the largest and second-largest spectrum values in the Fast Fourier Transform is equal to one. Second, the distance between k_{1st} and the averaged spectrum peak k_{ave} is required to be less than a certain value k_{dif} , which represents the only hyper-parameter in this algorithm as well as a parameter related to smoothness. **k_{ave} is the index that conveys the location of the spectrum peak averaged in short ranges, e.g., 2–30 range-bins from the lidar origin. Figure 5 shows a conceptual explanation of the variables of simplified Kalman gain in the cases of correct measurement and of an error peak.** In this study, the filtering algorithm is carried out first when the observation data is obtained:

$$K = \begin{cases} 1 & |k_{1st} - k_{2nd}| = 1 \text{ and } |k_{1st} - k_{ave}| < k_{dif} \\ 0 & \text{Otherwise} \end{cases} \quad (4)$$

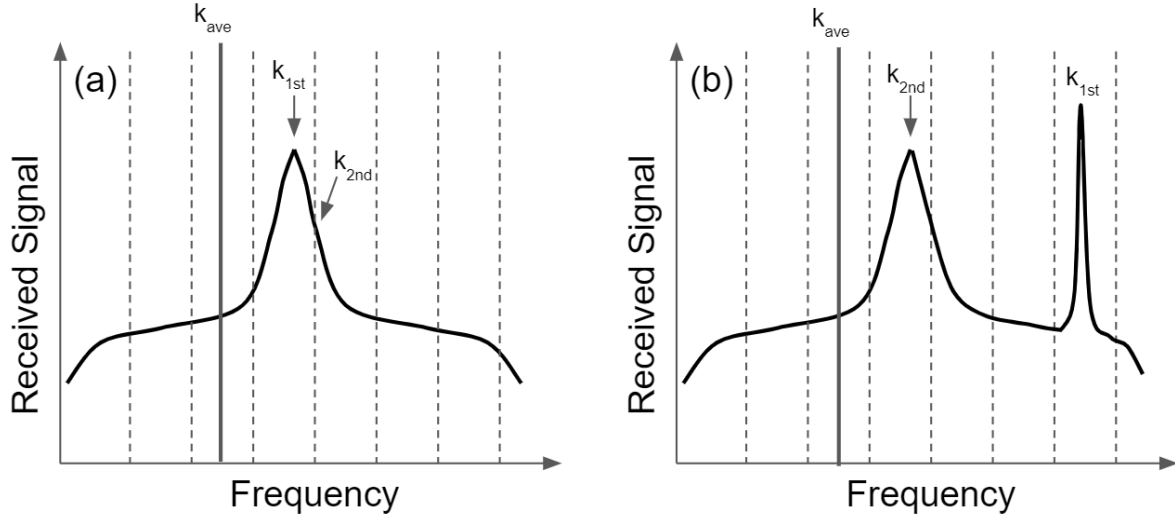


Fig. 5 Conceptual explanation of the variables of simplified Kalman gain.

(a) Correct measurement case of $K=1$. (b) Case with the error peak of $K=0$

208
209
210
211

212 Secondly, a robust least-squares estimation, based on Tuckey's biweight methodology (Huber, 2008), is
213 carried out to reduce the impact of the error in the LOS wind velocity. This method is based on the LOS wind data, in
214 contrast to the spectrum data from Lidar observations in the first method. Although the filtering algorithm based on a
215 simple Kalman filter can remove the error from the Lidar spectrum data, error filtering via this algorithm is not perfect
216 despite being useful. As error data can be a reason for miscontrol, it is essential to deal with the error and the loss of
217 data of the Lidars more carefully when the filtering algorithm is used for the preview control. Therefore, the robustness
218 of the estimated airflow vector is secured by combining the simple Kalman filtering algorithm with the results of
219 robust LSM, using Eqs. (2) and (3). In addition, the robust LSM estimation can employ the extrapolation algorithm
220 effectively as per Eqs. (2) and (3). Therefore, a simpler and more robust algorithm is provided. **Figure 6 explains the**
221 **concept behind Tuckey's biweight methodology as applied to Lidar. The fundamental principle involves comparing**
222 **the observed LOS wind values with the estimated ones from the polynomial expression used in the LSM. In the 1st**
223 **step, the LOS wind is estimated using the general LSM (Eq. (2)). In the 2nd step, the difference d_j^T between the**
224 **observed LOS wind value and that estimated from the polynomial expression is found:**

$$d_j^T = W_j^T - (a_j z + b_j). \quad (5)$$

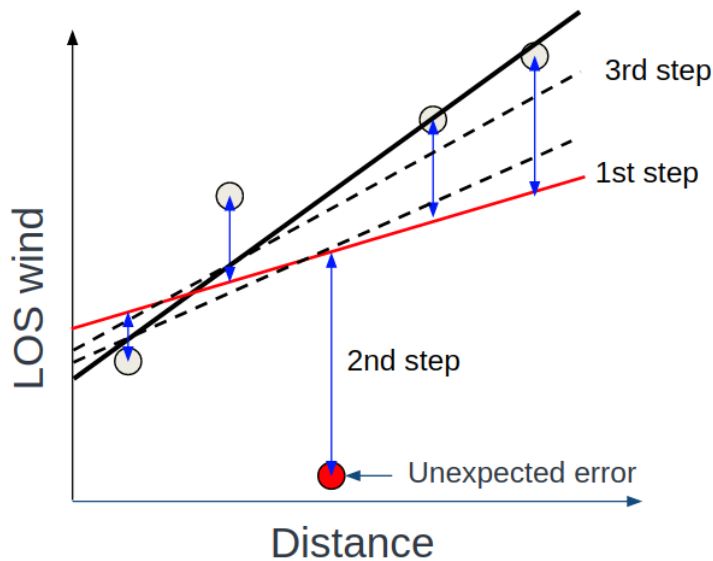
225 A permissible difference range L is defined and weights $w_j^T(d_j^T)$ are calculated depending on where d_j^T falls in the
226 distance range:

$$\begin{aligned} w_j^T(d_j^T) &= 0 \quad (d_j^T < -L) \\ w_j^T(d_j^T) &= \left(1 - \left(\frac{d_j^T}{w_j^T}\right)^2\right)^2 \quad (-L \leq d_j^T \leq L) . \\ w_j^T(d_j^T) &= 0 \quad (d_j^T > L) \end{aligned} \quad (6)$$

227 Weights are assigned to each LOS wind velocity value. In the 3rd step, a new first-degree polynomial expression for
 228 the LSM with the weighted data is estimated as follows.
 229

$$\begin{aligned}
 a_j' &= \frac{\sum_{i=T-(N-1)}^T w_j^i \sum_{i=T-(N-1)}^T w_j^i z^i W_j^i - \sum_{i=T-(N-1)}^T w_j^i z^i \sum_{i=T-(N-1)}^T w_j^i W_j^i}{\sum_{i=T-(N-1)}^T w_j^i \sum_{i=T-(N-1)}^T w_j^i (z^i)^2 - \left(\sum_{i=T-(N-1)}^T w_j^i z^i\right)^2} \\
 b_j' &= \frac{\sum_{i=T-(N-1)}^T w_j^i z^i \sum_{i=T-(N-1)}^T w_j^i W_j^i - \sum_{i=T-(N-1)}^T w_j^i z^i W_j^i \sum_{i=T-(N-1)}^T w_j^i z^i}{\sum_{i=T-(N-1)}^T w_j^i \sum_{i=T-(N-1)}^T w_j^i (z^i)^2 - \left(\sum_{i=T-(N-1)}^T w_j^i z^i\right)^2}
 \end{aligned} \tag{7}$$

230 This process is repeated until the weight of the error value decreases and converges.
 231



232
 233 **Fig. 6 Conceptual explanation of Tuckey's biweight methodology applied to line-of-sight (LOS) wind at various distances.**
 234 **First step: simple least-squares fit. Second step: observations are compared with the estimate. The data are weighted, and**
 235 **extreme outliers are excluded, using Eq. (6). Third step: Least-squares fit of the weighted data.**

236
 237
 238

2.4 Filtering Wind-Velocity Noise

240 Lidar is subject not only to measuring errors and loss of LOS data values but also to random noise; this type
 241 of noise also leads to a poor estimation of the airflow vector. **The random noise is caused by the reduced intensity of**
 242 **the received light due to the thin aerosol concentration in the sky. A general Lidar signal consists of random noise**
 243 **superimposed on the spectral signal. If the signal intensity is low, peak search may only detect the random noise.**
 244 **(Additional randomness caused by environmental factors and data processing in Lidar is considered here as**
 245 **randomness of the wind-speed values.)**

246 A simple spline algorithm generates a curve that passes through all sample points; therefore, it is not able to
247 generate a smooth curve when the sample points have random noise, and a smoothing spline algorithm is often applied
248 to remove the random noise in the Lidar LOS wind values, as in the study by Woltring, 1986. The curve generated by
249 this algorithm does not pass through all sample points, and because of that, it can be smoother, even when there is
250 random noise from Lidar LOS wind measurements. The smoothing spline model minimizes the criterion function C_p ,

$$C_p = \sum_{i=1}^n v_i \{y_i - s_p(x)\}^2 + p \int \left(\frac{d^2 s_p}{dx^2} \right)^2 dx, \quad (8)$$

251 where y_i is a sample point value, $s_p(x)$ is the value generated by a simple spline algorithm, v_i is a weighted factor, and
252 p is the regularization parameter. The smoothest curve is generated when the criterion function C_p is minimized.
253

254 2.5 System Flowchart

255 The airflow-vector estimation algorithm is a sequence of five different processes, which are summarized
256 below. The system flowchart is shown in [Fig. 7](#).

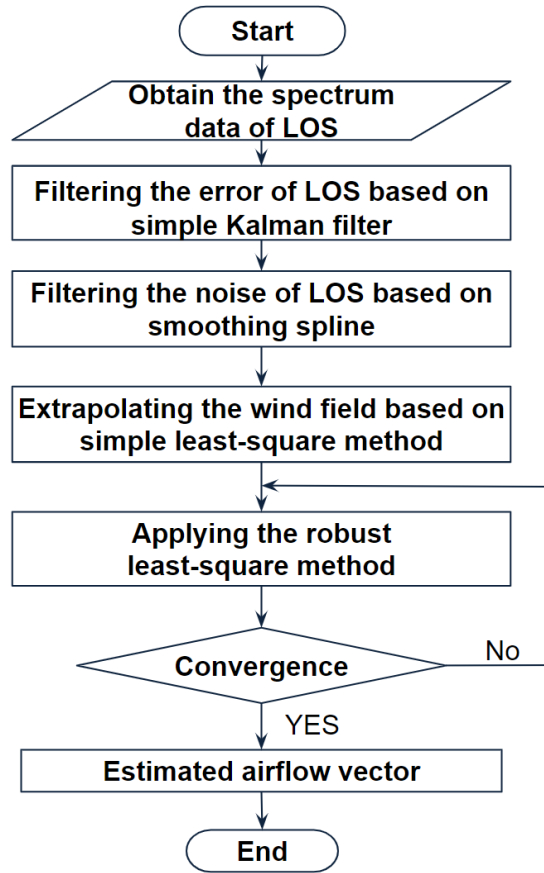
257 1) The filtering algorithm based on a simple Kalman filter is used to remove the error in Lidar LOS
258 wind-data values.

259 2) The smoothing spline method is applied to reduce the negative effect of the random noise in LOS
260 wind-data values and extrapolates the values at positions for which no measurements can be read. This is identified
261 as the first-step error.

262 3) Extrapolation, based on the polynomial expression, is carried out to estimate the wind-field values
263 by using current and past LOS wind data.

264 4) A robust LSM model is applied to obtain a more accurate polynomial expression. The calculation
265 repeats until the parameter converges.

266 5) The airflow vector is calculated by Eq. (1) with the extrapolated LOS wind.



267

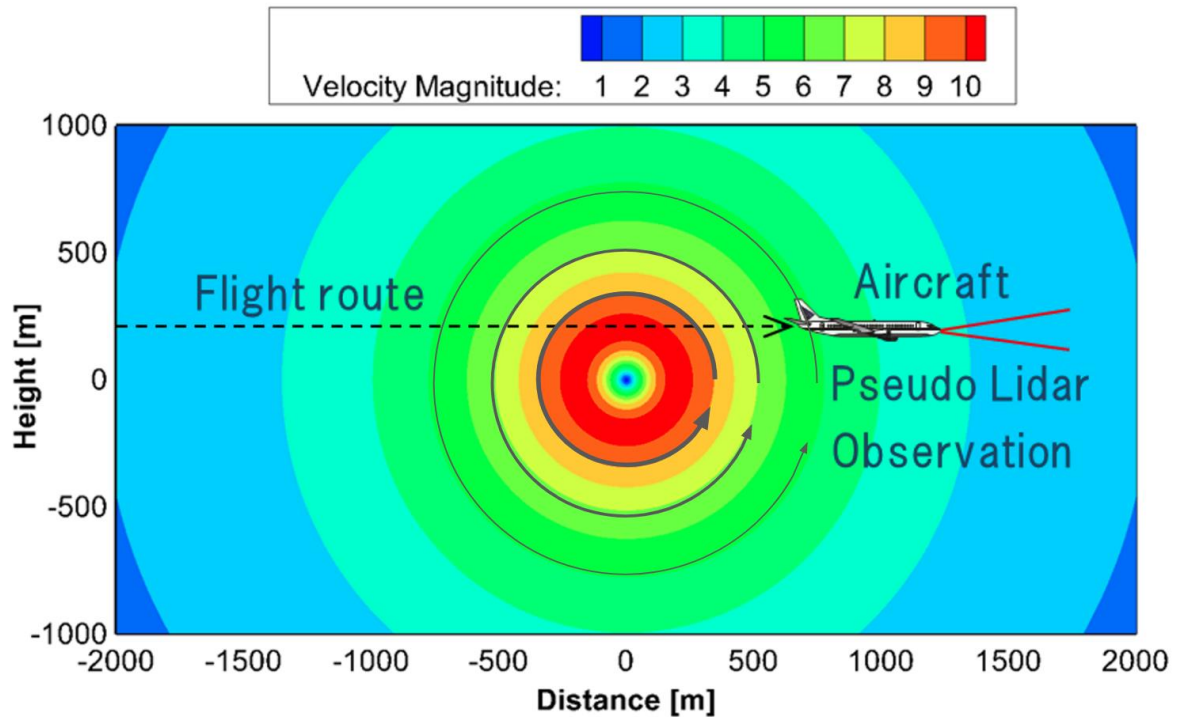
268

Fig. 7 System flowchart for the airflow vector estimation algorithm

269 3 Test Configurations

270 3.1 Ideal Vortex Model

271 We have conducted numerical experiments to evaluate the performance of actual airborne Lidars. The ideal
 272 vortex model is defined and used to evaluate the estimated performance of the airflow vector. In this study, the
 273 Hallock-Burnham vortex model (Hinton et al., 1997) is used. The experiment generates a large number of pseudo-
 274 Lidar values, from which the airflow vector is estimated. The estimation results are then compared with the reference
 275 wind-field values of the ideal vortex model. **Figure 8** shows the distribution of wind velocity generated using the
 276 Hallock-Burnham vortex model.



277
278 **Fig. 8 The distribution of vertical wind velocity generated by the Hallock-Burnham vortex model**

279
280 **3.2 NWP model**

281 The results predicted by a numerical weather model—the Japan Meteorological Agency Non-Hydrostatic
282 Model (JMA-NHM)—are used to evaluate airflow-vector estimation performance (Saito et al., 2007; Kikuchi et al.,
283 2015). To obtain high-resolution weather prediction, a one-way multi-nesting technique (Kikuchi et al. 2015) is
284 employed for downscaling purposes. The computational domain is nested four times to increase grid resolutions from
285 5.0 to 0.05 km gradually (in the sequence 5.0, 1.5, 0.5, 0.15, and 0.05 km).

286 Three-hour mesoscale objective analysis data, collected using a mesoscale four-dimensional variational data-
287 assimilation system at the Japan Meteorological Agency (Saito et al., 2007), are used for the initial condition of 5.0
288 km grid resolution. The experiment generates a large number of simulated twin-Lidar observation values along flight
289 routes from the wind-field data generated by JMA-NHM, which are more realistic than ideal-vortex model results.
290 The airflow vector is estimated from the pseudo-Lidar observations and compared with the JMA-NHM reference field.

291 **Figure 9 shows the distribution of the vertical wind velocity values generated by JMA-NHM.**

292

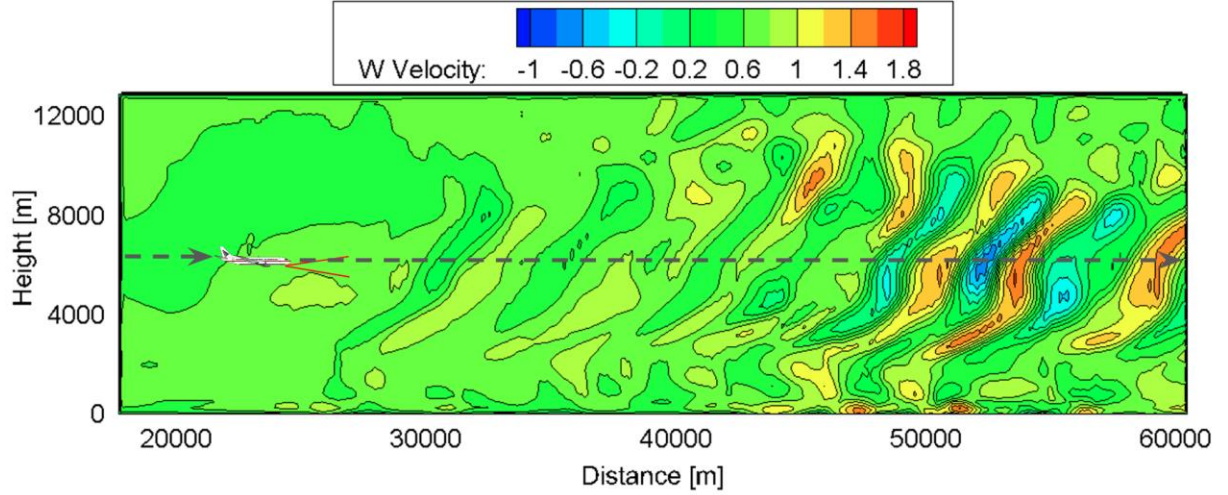


Fig. 9 Vertical wind velocity distribution map generated by JMA-NHM

3.3 Generation of pseudo-errors and noise

To confirm the effectiveness of the proposed filtering algorithms, errors and noise are generated artificially by using the parameter of the backscattering coefficient in the atmosphere and the statistics-based coherent Lidar equation (Kameyama et al., 2007). The backscattering coefficient is strongly related to the aerosol density in the atmosphere, and it has an impact on the Lidar measurements and estimation performance. When the backscattering coefficient is very low, the measurement performance is worse, and the LOS wind data show errors and noise. Apart from this, the measurement performance is related to the focal distance, pulse width, and Lidar power (Kameyama et al., 2007). The signal-noise ratio (SNR) at the receiver, at each LOS distance, is calculated by using the coherent Lidar equation and the detailed operating condition of JAXA's Lidar (Inokuchi and Akiyama 2019):

$$SNR(R) = \frac{\eta P_t \Delta R \beta K^{2R} \pi D^2}{h f B SRF(R)} \quad (9)$$

$$SRF(R) = 1 + \left\{1 - \frac{R}{F}\right\}^2 \left\{\frac{k(A_c D)^2}{8R}\right\}^2 + \left\{\frac{A_c D}{2S_0(R)}\right\}^2 \quad (10)$$

$$S_0(R) = (1.1 k^2 R C_n^2)^{-\frac{3}{5}} \quad (11)$$

Here, R is the observation distance, η is the system efficiency, P_t is the light-transmission power, ΔR is the resolution range, β is the backscattering coefficient, K is the atmospheric transmittance, D is the opening size of the optical antenna, h is Planck's constant, f is optical frequency, B is received bandwidth, F is focal distance, k is wave number, A_c is the vignetting factor of the optical antenna, and C_n^2 is the atmospheric structure constant. In this study, the conditions are set according to the design specification for airborne Lidars. Six atmospheric conditions are prepared in order to evaluate the filtering performance. The backscattering coefficients are (standard case) $1.8 \times 10^{-8} \text{ sr}^{-1}\text{m}^{-1}$, (a) $1.8 \times 10^{-11} \text{ sr}^{-1}\text{m}^{-1}$, (b) $1.35 \times 10^{-11} \text{ sr}^{-1}\text{m}^{-1}$, (c) $0.9 \times 10^{-11} \text{ sr}^{-1}\text{m}^{-1}$, (d) $0.45 \times 10^{-11} \text{ sr}^{-1}\text{m}^{-1}$, and (e) $0.18 \times 10^{-11} \text{ sr}^{-1}\text{m}^{-1}$. Figure 10 shows the statistics for the error and noise as functions of SNR bandwidth.

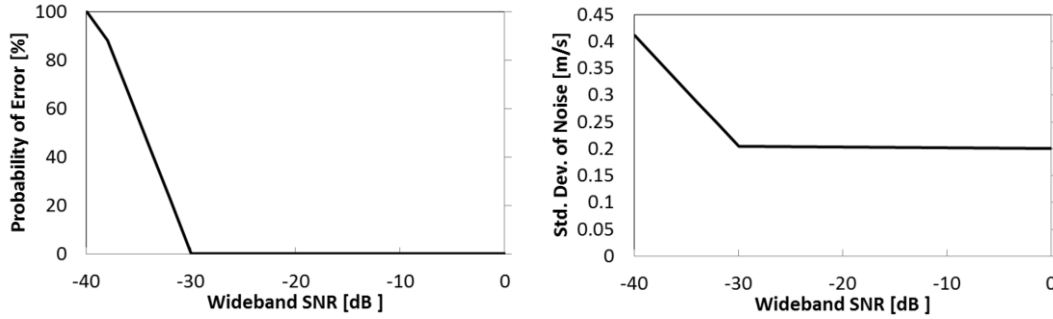


Fig. 10 Probability of error and standard deviation of noise as functions of signal-noise ratio (SNR) bandwidth

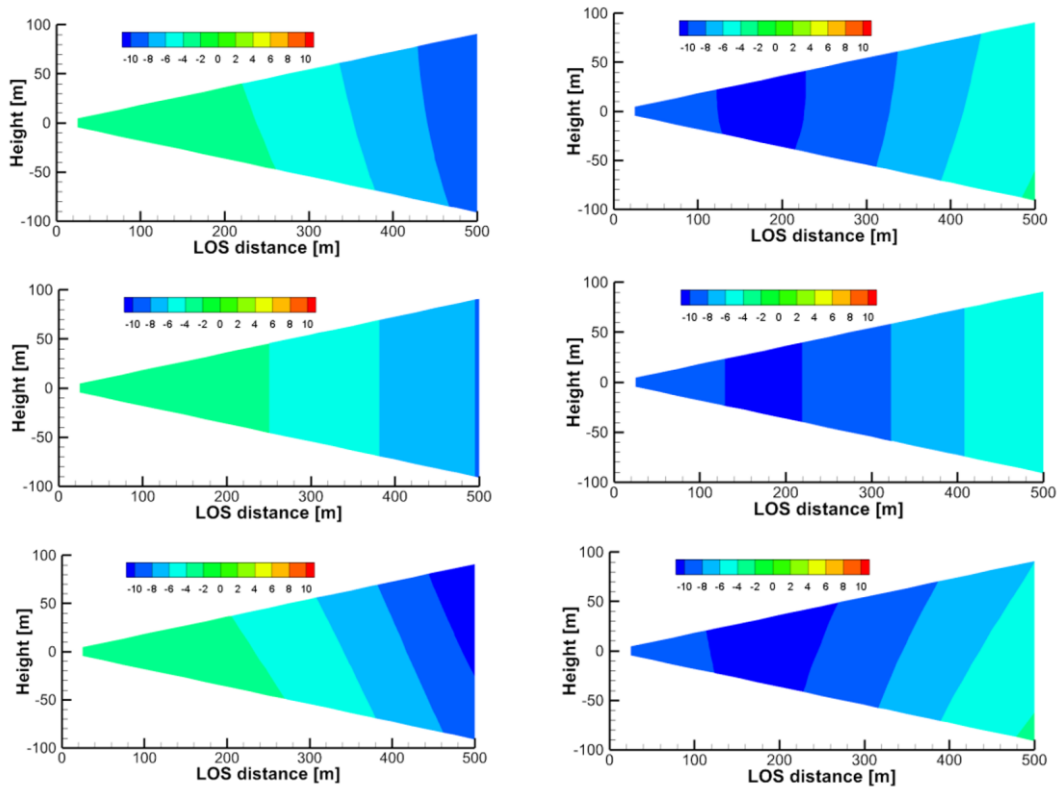
4 Results

4.1 Ideal Vortex Model without Error and Noise

The numerical experiments with the ideal vortex model have been carried out, and Figs. 11 and 12 show the distributions of the horizontal and vertical wind components that are estimated by the simple vector conversion and the proposed method. The flights start at the edge of the computational space. Figs. 11 and 12 show the results after 10 and 15 s, respectively. Thus, they represent the instants of time before and during the aircraft's close approach to the vortex core. As shown in Figs. 11 and 12, the simple vector conversion method, which assumes that the wind field of the region between the Lidars is homogeneous, cannot accurately reproduce the two-dimensional distribution between the Lidars. On the other hand, the figures confirm that the proposed method can estimate the two-dimensional distribution of wind-field values between the Lidars. Figure 11 shows that the two-dimensional distribution obtained with the proposed method is very similar to that of the reference field. In addition, the results show that the horizontal wind velocity with simple vector conversion is approximately -7 m/s, whereas that with the proposed method is -9.5 ms^{-1} ; the horizontal wind velocity of the reference field is -9.0 ms^{-1} at LOS distance of 450–500 m. Figure 12 shows that the results of the horizontal and vertical wind velocities with simple vector conversion are considerably lower than those of the reference field. The horizontal wind results show that the value obtained with the simple vector conversion is approximately -9.5 ms^{-1} , whereas that with the proposed method is approximately -3.5 ms^{-1} ; the horizontal wind velocity of the reference field is approximately -4.5 ms^{-1} at LOS distance of 450–500 m. The vertical wind results show that the value obtained with simple vector conversion is approximately -1.0 m/s, whereas that obtained with the proposed method is approximately 8.5 ms^{-1} ; the vertical wind velocity of the reference field is approximately 7.0 ms^{-1} at LOS distance of 450–500 m. Therefore, simple vector conversion has significantly large errors between the reference and estimated values. The errors in both the horizontal and vertical wind values estimated by the proposed method are much smaller than those estimated with simple vector conversion. Although the two-dimensional distribution of the horizontal wind-field values of the proposed method is larger than that of the reference field at a LOS distance of 450–500 m, the vertical wind-field values can provide a good assessment of the reference field shown in Fig. 12. The 15 s timing in Fig. 12 is a more challenging case than others because the aircraft is positioned very close to the center of the vortex, and the wind direction changes abruptly. Although it is difficult to

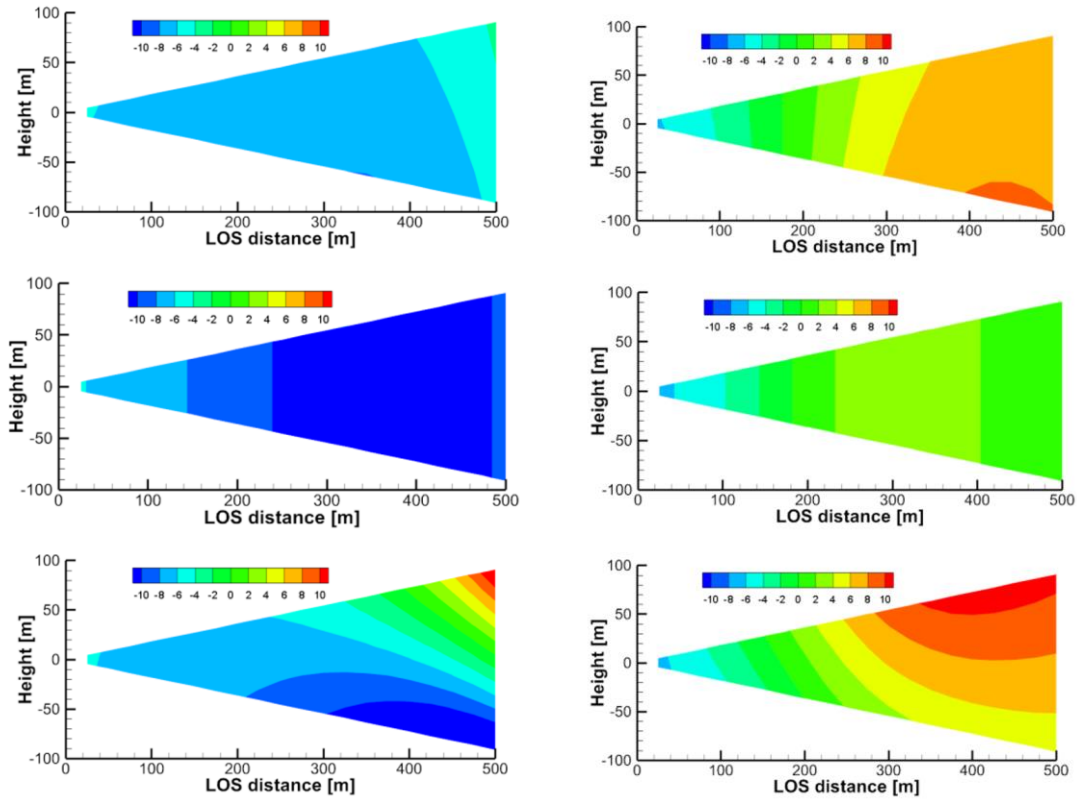
342 estimate the perfect wind-field value at this time by using the proposed method, the proposed estimation method
 343 demonstrably has a much higher accuracy than simple vector conversion. Overall, the proposed method has much
 344 better performance than the simple vector conversion method, and it can estimate the two-dimensional distribution of
 345 wind field values accurately, unlike the simple vector conversion method.

346 **Next, the statistical estimation performance is evaluated using 100 pseudo-routes that are randomly generated**
 347 **750 m above and below the center of the vortex core; Fig. 13 shows the results for the vertical wind values, along with**
 348 **the performance required for automatic control. The root mean square error (RMSE) between the reference-field value**
 349 **and the estimated wind-field value is used for evaluating the estimation performance. Moreover, the effect of the**
 350 **number of past Lidar observations used to determine the wind field, i.e., the past LOS wind, is checked. Simple vector**
 351 **conversion cannot satisfy the performance requirement at a LOS distance greater than 350 m. This means that**
 352 **achieving preview control using the simple vector conversion method may be difficult. At a LOS distance of 500 m,**
 353 **the RMSEs of the vertical wind values of the simple vector conversion and proposed methods are approximately 4.0**
 354 **ms⁻¹ and 1.2 ms⁻¹, respectively. The proposed method can cater to the performance demand even if the number of past**
 355 **LOS wind values used is different; a lower number leads to better estimation performance.**



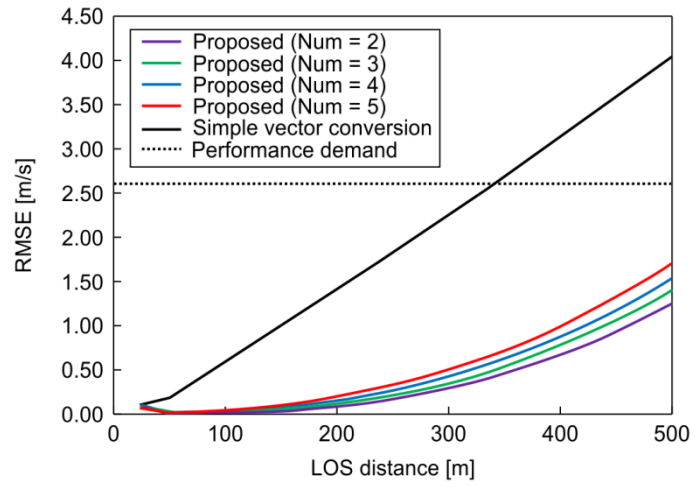
356
 357 **Fig. 11 Distributions of the horizontal and vertical wind components estimated by the simple vector conversion method**
 358 **vs. the proposed method (at time 10 s). Upper figures: ideal vortex model; middle figures: simple vector conversion**
 359 **method; lower figures: proposed method with five-past LOS wind datasets. Left figures: horizontal wind values; right**
 360 **figures: vertical wind values**

361



362
363
364
365
366

Fig. 12 Distributions of the horizontal and vertical wind components estimated by the simple vector conversion method vs. the proposed method (at time 10 s). Upper figures: ideal vortex model; middle figures: simple vector conversion method; lower figures: proposed method with five-past LOS wind datasets. Left figures: horizontal wind values; right figures: vertical wind values



367
368
369

Fig. 13 Statistical estimation performance (root mean square error) of vertical wind values (ideal vortex model). Num = number of past line-of-sight (LOS) wind values used

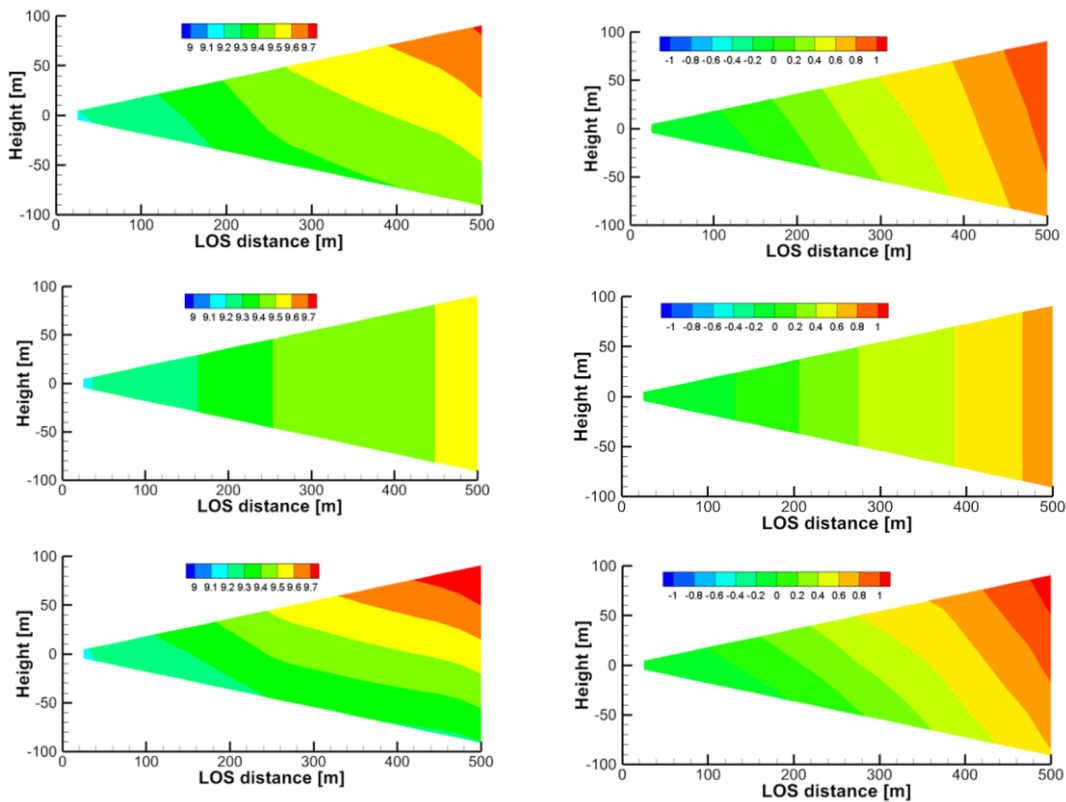
370 **4.1 Numerical Weather Prediction without Error and Noise**

371 We also conducted numerical experiments with NWP values. Figs. 14 and 15 show the distributions of the
372 horizontal and vertical wind components that are estimated by simple vector conversion and the proposed method.

373 Figure 14 shows the results for the instants of time **before and during the approach to a vertical wind fluctuation**. The
 374 simple vector conversion method cannot accurately reproduce the two-dimensional distribution of the wind field
 375 between the Lidars. On the other hand, the proposed method can estimate the two-dimensional distribution of the wind
 376 field between the Lidars more accurately. Figure 15 shows that the wind velocities predicted by the simple vector
 377 conversion method are higher than the reference fields at 300-500 m of LOS distance, in contrast to those of the
 378 proposed method.

379 **Next, the statistical estimation performance is evaluated using 100 pseudo-routes that are randomly generated**
 380 **between 2 km and 10 km altitude**. Fig. 16 shows the results, along with the performance requirement for automatic
 381 control. The effect of the number of past LOS wind-values used is also checked. In this case, both simple vector
 382 conversion and the proposed method can satisfy the performance demand for preview control; however, the
 383 performance results of simple vector conversion are much worse than those of the proposed method. Moreover, the
 384 proposed method can estimate quite accurate wind-field values. In this case, the use of a higher number of past LOS
 385 wind values leads to better estimation performance.

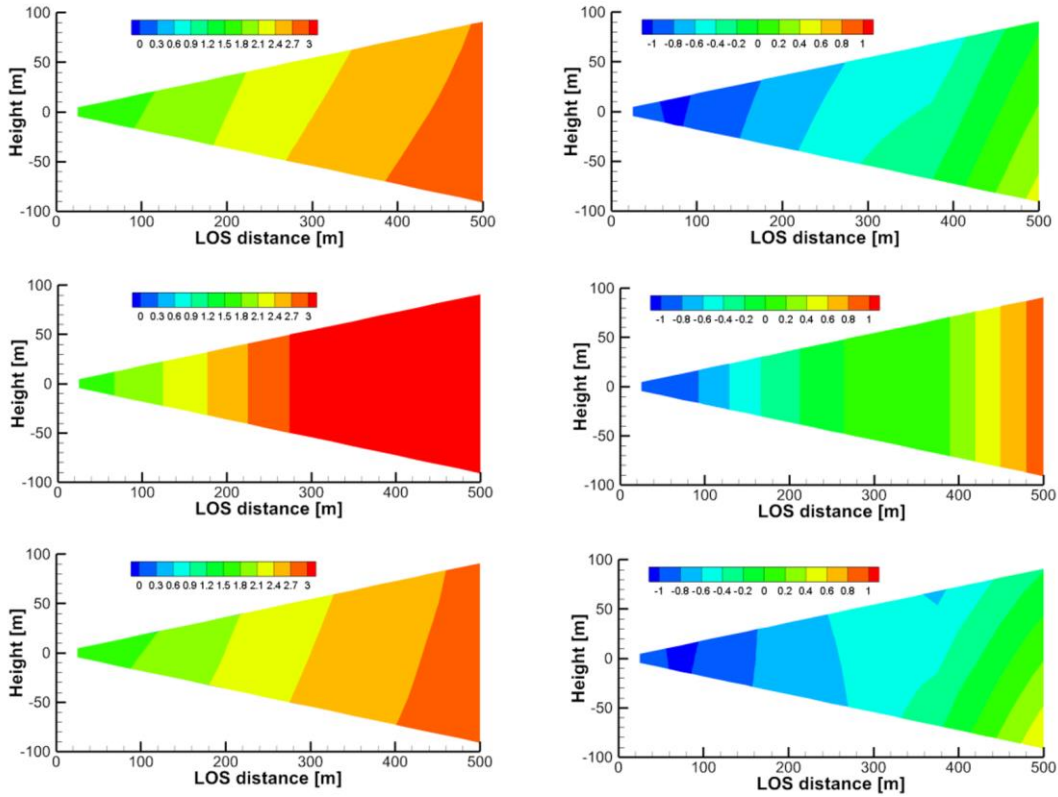
386



387

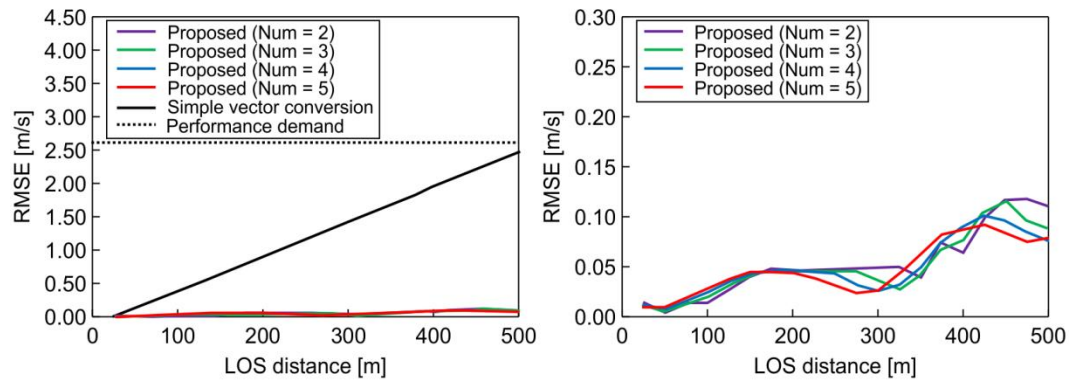
388 **Fig. 14 Distributions of horizontal and vertical wind components estimated via simple vector conversion and proposed**
 389 **method before approach to vertical wind fluctuation. Upper figures: ideal vortex model; middle figures: simple vector**
 390 **conversion method; lower figures: proposed method with five-past LOS wind datasets. Left figures: horizontal wind**
 391 **values; right figures: vertical wind values**

392



393
 394 **Fig. 15 Distributions of horizontal and vertical wind components estimated via simple vector conversion and proposed**
 395 **method immediately during approach to vertical wind fluctuation. Upper figures: ideal vortex model; middle figures:**
 396 **simple vector conversion method; lower figures: proposed method with five-past LOS wind datasets. Left figures:**
 397 **horizontal wind values; right figures: vertical wind values**

398



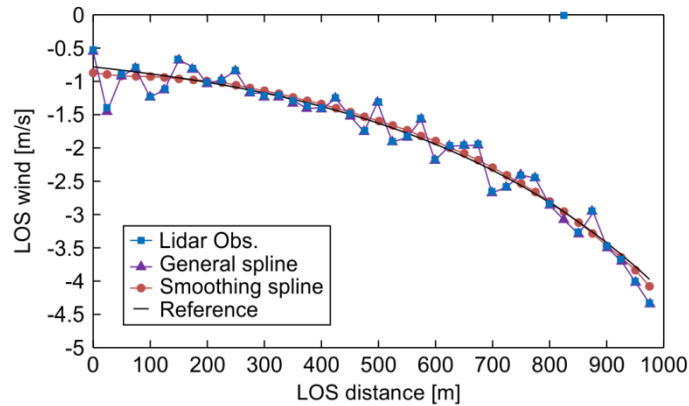
399
 400 **Fig. 16 Statistical estimation performance (root mean square error) for numerical weather prediction results. Num =**
 401 **number of past line-of-sight (LOS) wind values used**

402 4.2 Ideal vortex model with error and noise

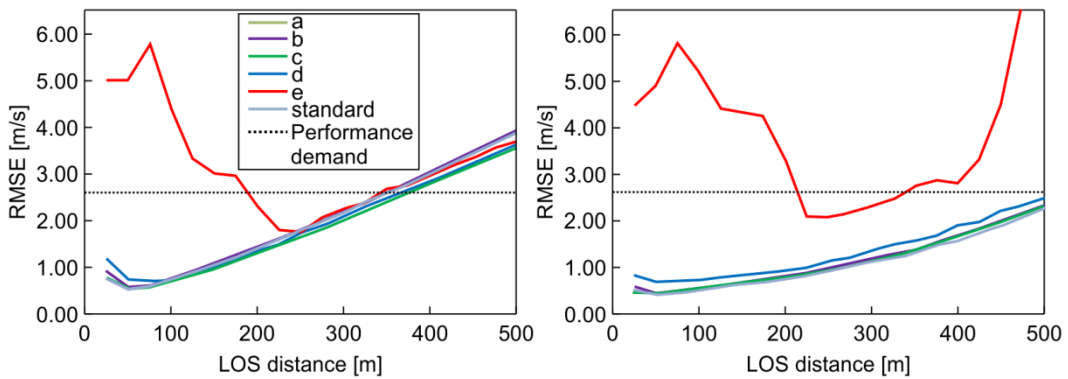
403 In this section, numerical experiments with error and noise in LOS wind values are conducted to evaluate the
 404 estimation performance of the proposed method. These numerical experiments show the error/noise-filtering

405 performance difference between simple vector conversion and the proposed method with extrapolation from the past
 406 LOS wind. Six atmospheric conditions are prepared in order to evaluate the filtering performance. The backscattering
 407 coefficients are (standard case) $1.8 \times 10^{-8} \text{ sr}^{-1} \text{ m}^{-1}$, (a) $1.8 \times 10^{-11} \text{ sr}^{-1} \text{ m}^{-1}$, (b) $1.35 \times 10^{-11} \text{ sr}^{-1} \text{ m}^{-1}$, (c) $0.9 \times 10^{-11} \text{ sr}^{-1} \text{ m}^{-1}$, (d)
 408 $0.45 \times 10^{-11} \text{ sr}^{-1} \text{ m}^{-1}$, and (e) $0.18 \times 10^{-11} \text{ sr}^{-1} \text{ m}^{-1}$.

409 First, numerical experiments with the ideal vortex model are carried out. Figure 17 shows the LOS wind
 410 values, which include the measured data with error and noise, the reference wind, the smoothing spline, and the general
 411 spline model results. Figure 17 shows that the smoothing spline can filter the error and noise data of LOS wind values.
 412 When the general spline is used, the error can be filtered correctly by using a simple Kalman filter and a robust LSM;
 413 however, the noise cannot be filtered. Next, the statistical estimation performance is evaluated using 100 pseudo-
 414 routes that are randomly generated 750 m above and below the center of the vortex core. Fig. 18 shows the results of
 415 the statistical estimation performance with error and noise. In addition, the difference due to the atmospheric
 416 conditions in the six cases with different backscattering coefficients is also checked. Simple vector conversion cannot
 417 satisfy the performance demand at a distance farther than 350 m LOS and cannot work correctly under atmospheric
 418 condition (e). The proposed method can always satisfy the performance demand except under atmospheric condition
 419 (e). It thus shows much better performance than simple vector conversion, even though it is difficult to estimate the
 420 wind field values by either method for atmospheric condition (e), which contains much larger noise levels than the
 421 other conditions.



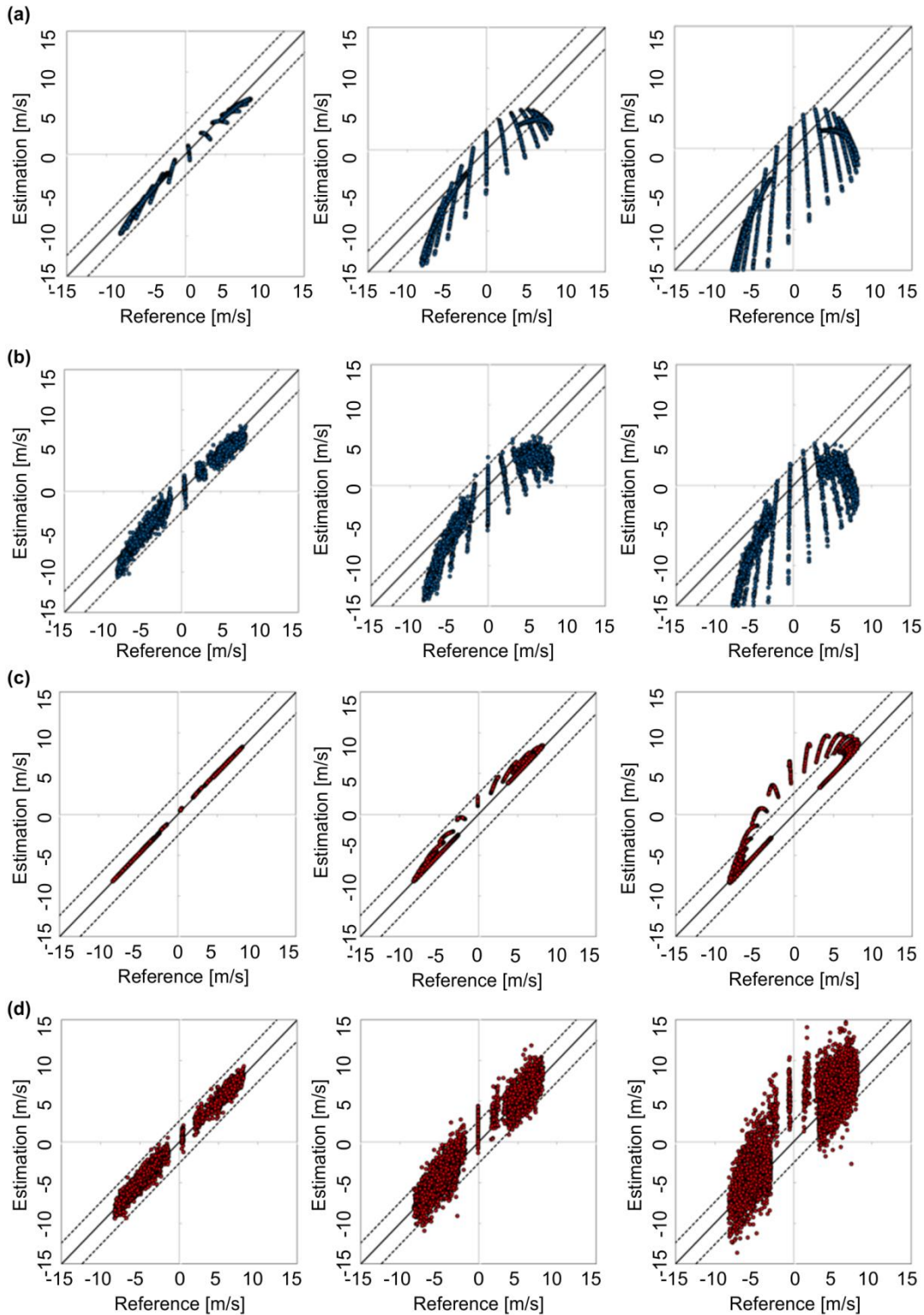
422
 423 **Fig. 17 Line-of-sight (LOS) wind values: measured data with error and noise, reference wind, smoothing spline, and**
 424 **general spline**



425

426 **Fig. 18 Statistical estimation performance (root mean square error) for line-of-sight (LOS) wind velocities including error**
427 **and noise under six atmospheric-condition scenarios (a–e and standard) (assuming ideal vortex model). Left figure:**
428 **simple vector conversion; right figure: proposed method**

429 In addition, the cross-plots of the reference and the estimated vertical wind are shown as Fig. 19. In Figs. 19
430 (a) and (b) the results of the simple vector conversion are presented; (c) and (d) show the results of the proposed
431 method. Figs. 19 (a) and (c) are the cases without error and noise, **whereas (b) and (d) are the cases with error and**
432 **noise**. By comparing (a) and (c), we can deduce that the proposed method provides a much better estimation than does
433 simple vector conversion. The results in (b) and (d) are spread wider than those in (a) and (c), because of the noise
434 data of LOS wind values. It is worth mentioning that the noise data have more negative effects on the result at 500 m
435 LOS distance than at 100 m and 300 m LOS. Nevertheless, comparison of (b) and (d) shows that the proposed method
436 can provide more accurate estimations than the simple vector conversion method.



437

438 **Fig. 19** Cross-plots of the reference and the estimated vertical wind data. Left figures: 100 m line-of-sight (LOS) distance;
 439 middle figures: 300 m LOS distance; right figures: 500 m LOS distance. (a), (b): Simple vector conversion; (c), (d):
 440 proposed method. (a), (c): cases without error and noise; (b), (d): cases with error and noise. The dots indicate the wind
 441 speed estimated at 5 Hz, and the dotted lines indicate the performance demand for control.

442

4.3 Numerical weather prediction with error and noise

We also carry out numerical experiments with NWP. The statistical estimation performance is conducted by using 100 pseudo-routes between 2 km and 10 km altitude. Fig. 20 shows the results of the statistical estimation performance with error and noise. Six different atmospheric conditions (standard, (a), (b), (c), (d), and (e), defined by their backscattering coefficients) are used. In this case, both simple vector conversion and the proposed method can satisfy the performance requirement for preview control; however, the simple vector conversion shows worse performance than the proposed method. The proposed method can estimate wind-field values quite accurately and displays better performance than the simple vector conversion method. As in the previous experiment, it is difficult to estimate the wind field-values for atmospheric condition (e) by using either simple vector conversion or the proposed method.

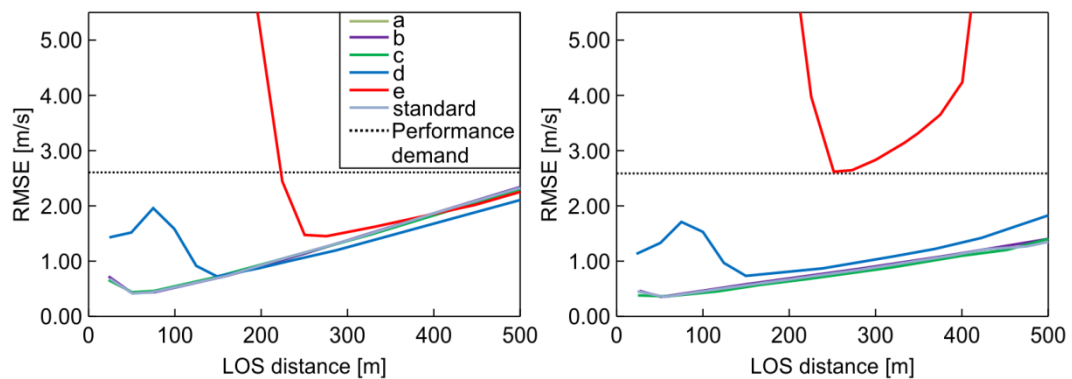


Fig. 20 Statistical estimation performance (root mean square error) for line-of-sight (LOS) wind velocities (including error and noise) under six atmospheric-condition scenarios (a–e and standard) with numerical weather-prediction data. Left figure: simple vector conversion; right figure: proposed method

5. Conclusion

In this study, an airflow vector estimation algorithm based on upward and downward airborne Lidars has been proposed for preview control to prevent turbulence-induced aircraft accidents. This estimation algorithm uses the technique of extrapolating the wind-field values by using the LSM and the current and past LOS wind datasets to improve the accuracy of estimated wind values. Two test configurations for numerical experiments (ideal vortex flow and realistic NWP weather field values) have been used to evaluate the estimation of the airflow vector.

Numerical experiments on LOS wind estimation show that the proposed extrapolation method has much better performance than simple vector conversion methods, and it can estimate the two-dimensional distribution of wind-field values accurately, which simple vector conversion cannot. The estimation performance and the computational cost of the proposed method can satisfy the performance demand for preview control.

Numerical experiments with error and noise in the LOS wind data have been conducted to evaluate the performance of the proposed estimation method. These numerical experiments show that the smoothing spline model can filter noise correctly and reduce its negative effects. The proposed method performs much better than the simple vector conversion method, although it is difficult to estimate the wind-field values for atmospheric condition (e) with either method. Atmospheric condition (e) has more noise than other conditions, and when the noise exceeds a certain level, it becomes difficult to estimate the air flow regardless of the method applied.

473 The proposed algorithm can satisfy the performance demands for preview control in both estimation
474 performance and computational cost. It can estimate a two-dimensional distribution that cannot be estimated by
475 existing methods. This is valuable for improving the accuracy of the preview control: for example, the proposed
476 method can cope with the critical case where the flight direction of the aircraft is at a steep angle with the aircraft
477 either ascending or descending.

478 The findings of this study are subject to certain limitations. The target size of the atmospheric turbulence is
479 assumed by the proposed algorithm to be comparable to or larger than the observation region between the Lidars.
480 Therefore, it is difficult to estimate a wind field with turbulence smaller than this. The effect on the aircraft vibration
481 due to such minor turbulence, however, is minimal. **An exception to this is aircraft-generated wake turbulence, which
482 still poses a safety risk. The radius of the actively fluctuating wake-turbulence core is only a few meters, so the
483 proposed method could lead to erroneous predictions.** A second limitation is that the current results are obtained from
484 numerical experiments and not from evaluations of actual observations. **Currently, the Lidar system is being modified
485 to be smaller and lighter in order to suit small experimental aircraft. The onboard Lidar system and real-time airflow-
486 vector estimation will be validated by flight experiments in 2021; the whole gust-alleviation system, including preview
487 control, will be demonstrated in 2022. The results of this research will be applied to this flight demonstration.**

488
489

490 **Author Contributions**

491 Ryota Kikuchi, Takashi Misaka, and Shigeru Obayashi designed the experiments. Ryota Kikuchi performed
492 the experiments, developed the model code, performed the simulations, and prepared the manuscript with
493 contributions from all co-authors. Hamaki Inokuchi contributed to the analysis and interpretation of data related to
494 Lidar and assisted in the preparation of the manuscript. All authors approve the final version of the manuscript and
495 agree to be accountable for all aspects of the work in ensuring that questions related to the accuracy or integrity of any
496 part of the work are appropriately investigated and resolved.

497 **Competing Interests**

498 The authors declare that they have no conflict of interest.

499 **References**

500 Airbus S.A.S.: Flight Operations Briefing Notes: Adverse Weather Operations – Optimum Use of the Weather Radar,
501 available at: <https://safetyfirst.airbus.com/optimum-use-of-weather-radar/>, 2020, last access: 22 September 2020.
502
503 Barny, H.: DELICAT – Demonstration of Lidar Based Clear Air Turbulence Detection, in: Innovation for Sustainable
504 Aviation in a Global Environment: Proceedings of the Sixth European Aeronautics Days, 253, 2012.

505
506 Boeing Commercial Airplanes: Statistical Summary of Commercial Jet Airplane Accidents, 2018.
507
508 Federal Aviation Administration: Preventing injuries caused by turbulence 2006, available at:
509 https://www.faa.gov/regulations_policies/advisory_circulars/index.cfm/go/document.information/documentid/99831,
510 2020, last access: 23 September 2020.
511
512 Fezans, N., Joos, H.D., and Deiler, C.: Gust load alleviation for a long-range aircraft with and without anticipation,
513 CEAS Aeronautical Journal, 10, 1-25, 2019.
514
515 Hamada, Y.: New LMI-based conditions for preview feedforward synthesis, Control Engineering Practice, 90, 19-26,
516 2019
517
518 Hinton, D. A., and Tatnall, C. R.: A candidate wake vortex strength definition for application to the NASA aircraft
519 vortex spacing system (AVOSS), NASA Technical Reports, 1997.
520
521 Huber, P. J.: Robust Statistics, Springer, Berlin, Heidelberg, 2008.
522
523 Inokuchi, H.: Detection of the Clear Air Turbulence by an Airborne Doppler LIDAR, in: Proceedings of Asia-Pacific
524 International Symposium on Aerospace Technology, 2012.
525
526 Inokuchi, H. and Akiyama, T.: True airspeed measured by an airborne coherent doppler lidar, in: APISAT 2019: Asia
527 Pacific International Symposium on Aerospace Technology (p. 554), 2019.
528
529 Inokuchi, H., Tanaka, H., and Ando, T.: Development of an onboard doppler lidar for flight safety, Journal of Aircraft,
530 46(4), 1411-1415, 2009
531
532 International Air Transportation Association: Safety Report 2015, 2016.
533
534 Japan Transport Safety Board: 2003-2012: Aircraft accident reports, available at: <http://www.mlit.go.jp/jtsb/>, 2020,
535 last access: 23 September 2020.
536
537 Kikuchi, R., Misaka, T., and Obayashi, S.: Real-Time Flow Prediction of Low-Level Atmospheric Turbulence, in
538 33rd Wind Energy Symposium, 2015.
539
540 Kameyama, S., Ando, T., Asaka, K., Hirano, Y., and Wadaka, S.: Compact all-fiber pulsed coherent Doppler lidar
541 system for wind sensing, Applied Optics, 46(11), 1953-1962, 2007

542
543 Kim, J.H. and Chun, H.Y.: Statistics and possible sources of aviation turbulence over South Korea. *Journal of Applied*
544 *Meteorology and Climatology*, 50(2), 311-324, 2011.
545
546 Kim, J. H., Chun, H. Y., Sharman, R. D., and Keller, T. L.: Evaluations of upper-level turbulence
547 diagnostics performance using the Graphical Turbulence Guidance (GTG) system and pilot reports
548 (PIREPs) over East Asia, *Journal of Applied Meteorology and Climatology* 50(9), 1936-1951, 2011.
549
550 Kim, J. H., Chan, W. N., Sridhar, B., and Sharman, R. D.: Combined winds and turbulence prediction
551 system for automated air-traffic management applications, *Journal of Applied Meteorology and*
552 *Climatology* 54(4), 766-784, 2015.
553
554 Machida, S.: Project Overview of R&D for Onboard Turbulence Detection System, in: Proceedings of Asia-Pacific
555 International Symposium on Aerospace Technology 2017, Plenary Lecture 4, Seoul, Korea, 2017.
556
557 Misaka, T., Nakabayashi, F. K., Obayashi, S., and Inokuchi, H.: Filtering Algorithm of Airborne Doppler Lidar
558 Measurements for Improved Wind Estimation, *Transactions of the Japan Society for Aeronautical and Space Sciences*,
559 58(3), 149-155, 2015
560
561 Neininger, B.: Trends in airborne atmospheric observations, *European Meteorological Society Annual Meeting 2017*,
562 14, EMS2017-322, 2017
563
564 Newsom, R. K., et al.: Validating precision estimates in horizontal wind measurements from a Doppler lidar, US
565 Department of Energy, Office of Scientific and Technical Information, NREL/JA-5000-68401,
566 <https://doi.org/10.5194/amt-10-1229-2017>, 2017.
567
568 Regan, C.D., and Jutte, C.V.: Survey of applications of active control technology for gust alleviation and new
569 challenges for lighter-weight aircraft. NASA Technical Memorandum, NASA-TM-2012-216008, 2012.
570
571 Saito, K., Ishida, J. I., Aranami, K., Hara, T., Segawa, T., Narita, M., and Honda, Y.: Nonhydrostatic atmospheric
572 models and operational development at JMA, *Journal of the Meteorological Society of Japan* 85B, 271-304, 2007.
573
574 Sakimura, T., Watanabe, Y., Ando, T., Kameyama, S., Asaka, K., Tanaka, H., Yanagisawa, T., Hirano,
575 Y. and Inokuchi, H.: 3.2 mJ, 1.5 μ m laser power amplifier using an Er, Yb:glass planar
576 waveguide for a coherent Doppler LIDAR, in: Proceedings of 17th Coherent Laser Radar
577 Conference, Barcelona, Spain, 2013.
578

579 Schmitt, N. P., Rehm, W., Pistner, T., Zeller, P., Diehl, H., and Navé, P.: The AWIATOR airborne LIDAR turbulence
580 sensor, *Aerospace Science and Technology*, 11(7), 546-552, 2007
581

582 Sermi, F., Cuccoli, F., Mugnai, C., and Facheris, L.: Aircraft hazard evaluation for critical weather avoidance, in:
583 *IEEE Metrology for Aerospace (MetroAeroSpace)*, Benevento, Italy, 2015, 454-459, 2015.
584

585 **Sharman, R., Tebaldi, C., Wiener, G., and Wolff, J.: An integrated approach to mid-and upperlevel**
586 **turbulence forecasting, *Weather and Forecasting* 21(3), 268–287, 2006.**
587

588 Soreide, D. C., Bogue, R. K., Ehernberger, L. J., Hannon, S. M., and Bowdle, D. A.: Airborne coherent LIDAR for
589 advanced in-flight measurements (ACLAIM) flight testing of the LIDAR sensor, *NASA Technical Reports*, 2000.
590

591 **Wei, T., Xia, H., Hu, J., Wang, C., Shangguan, M., Wang, L., Jia, M. and Dou, X.: Simultaneous wind and rainfall**
592 **detection by power spectrum analysis using a VAD scanning coherent Doppler lidar, *Optics Express*, 27(22), 31235-**
593 **31245, 2019.**
594

595 **Williams, P.D.: Increased light, moderate, and severe clear-air turbulence in response to climate change, *Advances in***
596 ***Atmospheric Sciences*, 34(5), 576-586, 2017.**
597

598 Woltring, H. J.: A Fortran package for generalized, cross-validatorspline smoothing and differentiation, *Advances*
599 *in Engineering Software*, 8(2) 104-113, 1986.